




JGR Solid Earth

RESEARCH ARTICLE

10.1029/2022JB025458

Lithospheric Structure of the Red Sea Based on 3D Density Modeling: A Contrasting Rift Architecture

Ran Issachar¹ , Ángela María Gómez-García^{2,3,4} , and Jörg Ebbing¹ 

¹Institute of Geosciences, Kiel University, Kiel, Germany, ²GFZ German Research Centre for Geosciences, Potsdam, Germany, ³Corporation Center of Excellence in Marine Sciences (CEMarin), Bogotá, Colombia, ⁴Now at Geosciences Barcelona (GEO3BCN), CSIC, Barcelona, Spain

Key Points:

- Gravity modeling in the Red Sea suggests a contrasting rift architecture in the central-southern regions and in the northern regions
- In the central-southern regions, ultrawide margins and thinned continental crust are overlaid by a broad asthenosphere upwelling
- In the northern regions, we infer exhumed mantle lithosphere and a narrow asthenosphere upwelling

Supporting Information:

Supporting Information may be found in the online version of this article.

Correspondence to:

R. Issachar,
ranissachar@gmail.com

Citation:

Issachar, R., Gómez-García, Á. M., & Ebbing, J. (2023). Lithospheric structure of the Red Sea based on 3D density modeling: A contrasting rift architecture. *Journal of Geophysical Research: Solid Earth*, 128, e2022JB025458. <https://doi.org/10.1029/2022JB025458>

Received 23 AUG 2022

Accepted 21 APR 2023

Author Contributions:

Conceptualization: Ángela María Gómez-García, Jörg Ebbing
Formal analysis: Ran Issachar
Methodology: Ran Issachar, Ángela María Gómez-García, Jörg Ebbing
Software: Ran Issachar, Ángela María Gómez-García, Jörg Ebbing
Supervision: Jörg Ebbing
Validation: Jörg Ebbing
Visualization: Ran Issachar
Writing – original draft: Ran Issachar
Writing – review & editing: Ángela María Gómez-García, Jörg Ebbing

© 2023. The Authors.

This is an open access article under the terms of the [Creative Commons Attribution License](https://creativecommons.org/licenses/by/4.0/), which permits use, distribution and reproduction in any medium, provided the original work is properly cited.

Abstract The Red Sea is an ideal location for studying rifting processes, offering a young and active intra-continental rift at the final stages of breakup. We explore the 3D lithospheric structure of the Red Sea by analyzing the gravity response of four end-member models of rift architecture, including two end-member types margin architecture Type I—narrow margins and exhumed lithospheric mantle, and Type II—(ultra)wide margins and removal of lithospheric mantle. Additionally, we test two options for the distribution of the oceanic crust (a) limited, that is, confined only to regions of magnetic stripes, and (b) extended, that is, available in vast areas within the basin. South of latitude 23°N, our results suggest the presence of ultrawide margins and limited oceanic crust. North of this latitude, the model of exhumed mantle and limited oceanic crust has minimized residuals compared to the observed gravity field, and agrees with a previously published regional tomographic model. Additionally, we find evidence for the presence of a high-density body along the southern Arabian coast, probably associated with magmatic underplating. We discuss the lithospheric structure of the Red Sea with respect to the nearby Afar plume, agreeing that the close proximity of the central-southern regions to the plume promoted a reduction in the strength of the lithosphere, and led to the development of ultrawide margins in these areas.

Plain Language Summary The Red Sea is a young example of continental break-up, a process in which a continent disintegrate into smaller pieces and an ocean is formed between them. We explore the sub-surface structure of the Red Sea, down to 140 km, aiming to better understand the mechanisms that allowed the Arabian plate to separate from Africa ~23 million years ago. We examine the gravity response of four end-member models of rift structures and compare them to the gravity signal measured in this region. We find that the sub-surface structure in the central-southern region is different than in the northern regions. Toward the south, the crust is thin and stretched, the lithospheric mantle is absent, and the asthenosphere is rising in a wide region. In the north the lithospheric mantle is exhumed and the asthenosphere is rising in narrow regions below the center of the basin. We discuss the reasons for these differences and support the possibility that the Afar Plume, currently located to the south of the Red Sea, had a thermal weakening effect on the central-southern regions of the Red Sea, which allowed the lithosphere to deform more easily, having direct implications in the present-day architecture of the Red Sea.

1. Introduction

The lithospheric structure of successful rifts can shed light regarding the breakup process and the controlling factors of the architecture of conjugate margins. Studying ancient rifts is difficult because the prolonged geological history could overprint the spatial and temporal relations to geodynamic features, especially the activity of nearby plumes. Thus, to examine the breakup process and the influence of the proximity of mantle plumes on the rift architecture, a young and active case study is desired. The Red Sea offers a unique opportunity due to its young age and its close proximity to the Afar plume (Figure 1). Evidence for rifting are found along the Red Sea ~8 Myr after the massive deposition of the Ethiopian-Yemen traps, during the Early Oligocene (Bosworth et al., 2005; Stockli & Bosworth, 2018).

Even though many factors influence the modes of crustal thinning, numerical simulations showed that the rheology of the crust has a major influence on the final architecture of the rifted margins and may lead to the formation of contrasting end-member types of rifted margins (Brune et al., 2017; Buck, 1991; Huisman & Beaumont, 2014). Particularly, a strong crust can lead to a localized crustal thinning after a limited extension and to the formation

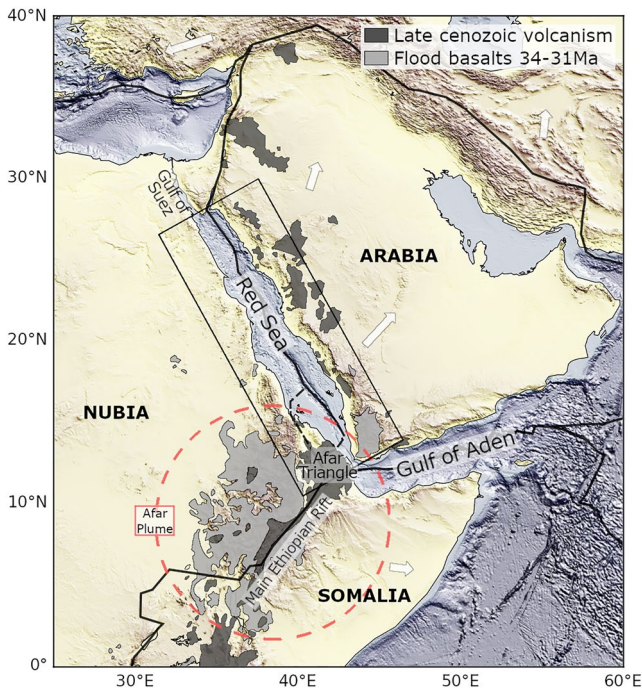


Figure 1. Tectonic setting of the study area showing the general plate configuration (from USGS (2021) and from Viltres et al. (2020) in the Afar region). Onshore volcanics are modified from Varet (1978), Davison et al. (1994), Beyene and Abdelsalam (2005) and Bosworth and Stockli (2016). Red dashed circle indicates the present-day Afar plume area. White arrows indicate GPS velocities with respect to Nubia (modified from Reilinger et al. (2006)). The black box indicates our modeling area.

of Type I margins, like in the case of the Iberia-Newfoundland conjugate margins (Péron-Pinvidic & Manatschal, 2009). This type of margin is outlined by narrow regions (less than about 100 km wide) of thinned continental crust and areas of exhumed (and serpentinized) continental mantle lithosphere along the continent-ocean transition (Huisman & Beaumont, 2011). On the contrary, a weak crust can lead to protracted crustal extension and to the formation of Type II margins, like in the case of the Brazil-Angola conjugate margins (Péron-Pinvidic et al., 2017). This type of margin is characterized by (ultra)wide regions (up to 500 km) of thin continental crust and the removal of the lithospheric mantle (Huisman & Beaumont, 2011). As expected, the proximity to a mantle plume has shown to lead to a reduction in the strength of the lithosphere, and thus, may influence the rifting process and the final architecture of the margins (Brune et al., 2013; Dang et al., 2020; François et al., 2018; Koptev et al., 2015). Moreover, the close spatial and temporal coincidence of rifts and plumes allowed previous studies to suggest that the latter has a decisive role in the continental breakup and even in the disintegration processes of supercontinents (Buitert, 2014; Courtillot et al., 1999; Morgan, 1971; Storey, 1995).

Several models aimed to link the rifting in the Red Sea with deep lithospheric processes, including asthenospheric flow derived rifting (Lowell & Geni, 1972), diffuse extension (Cochran, 1983) and magmatic expansion (Bohannon & Eittreim, 1991). However, these models relied on limited data that could not image the deep lithospheric structures. A recent seismic velocity model for the northern Red Sea revealed a narrow low-velocity anomaly along the rift axis, which was interpreted as an evidence for a transition from continental rifting to oceanic spreading (El Khrepy et al., 2021). However, the lithospheric structure along the central-southern Red Sea is still unknown.

In this study, we test four end-member models of the 3D lithospheric structure along the Red Sea (Figure 2), based on previously published geophysical data sets. We explore their gravity response, aiming to distinguish between end-member types of rifted margins following the classification presented in Huisman and Beaumont (2011): Type I—narrow margins outlined by exhumed continental mantle lithosphere and confined asthenosphere upwelling (Figures 2a and 2b); and

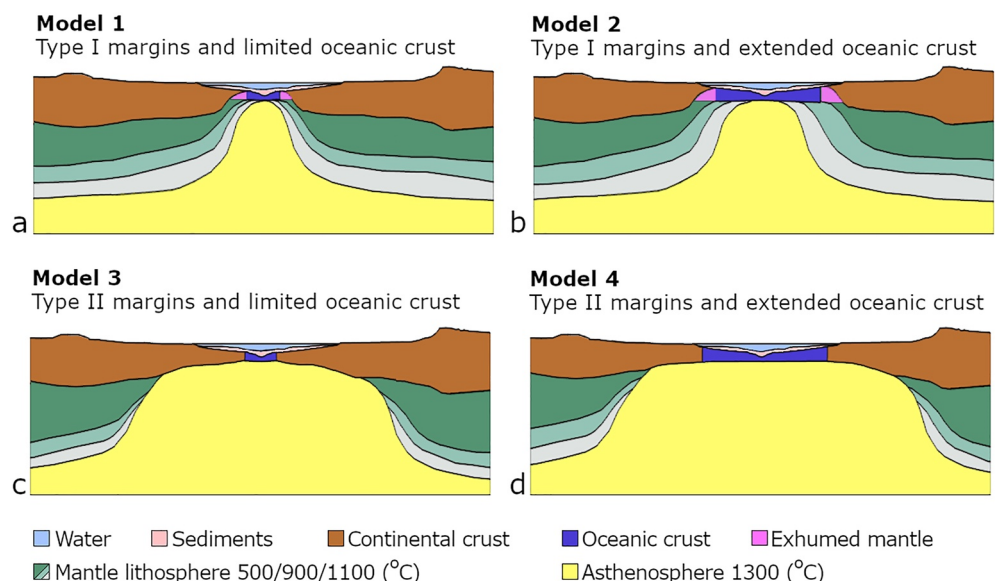


Figure 2. Schematic representation of the four end-member types of lithospheric structures tested in this study.

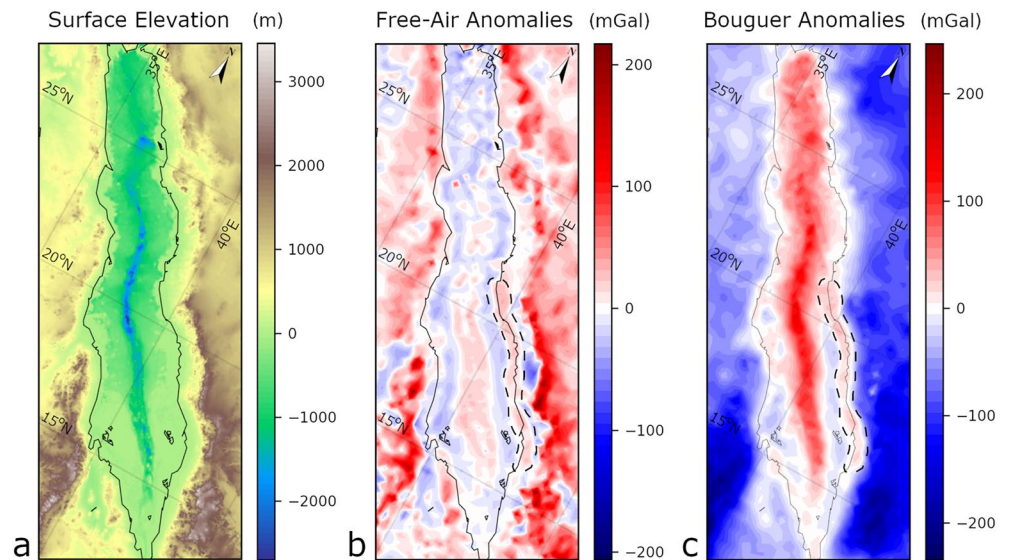


Figure 3. Data used in this study. (a) Surface elevation from GEBCO 2021 (GEBCO Compilation Group, 2021). (b) Free-air gravity and, (c) Bouguer gravity anomaly derived from the XGM2019e model (Zingerle et al., 2020). Dashed area denotes the positive gravity anomaly along the southern Arabian shoreline.

Type II—(ultra)wide margins outlined by removal of the mantle lithosphere and broad asthenosphere upwelling (Figures 2c and 2d). In addition, as the extent and age of the oceanic crust in the Red Sea is still a matter of debate (see Section 2.1), we include in our modeling two options for oceanic crustal distribution: limited—only where magnetic stripes are observed (Schettino et al., 2016); and extended—where segmentation trails are observed (Augustin et al., 2021) (Figure 4b). Lastly, we interpret our results considering other works about the seismic and thermal structure of the upper mantle in this area, that allow us to further discuss the influence of the Afar plume on the present-day rift architecture of the Red Sea.

2. Geological Setting

2.1. Morphology, Stratigraphy and Oceanic Accretion

The Red Sea is a ~2,000 km long intra-continental rift basin that cuts the Precambrian Arabo-Nubian shield and separates Arabia from Africa (Figure 1). It is part of the Afro-Arabian rift system, including the rifts of the Gulf of Aden and the Afar triangle. The Red Sea has a distinctive morphology, including elevated rift shoulders, narrow marginal shelves, a wide main trough and a deep and narrow axial trough (Figure 3a). In the regions southward of latitude 20°N, the coastal plains are rather wide and shallow. The main trough and the coastal plains are covered by ~6.5 km of sediments including open marine facies and massive evaporitic sequences (Bosworth et al., 2005). In the central and southern regions, the axial basaltic seafloor of tholeiitic composition is exposed (Altherr et al., 1990; Haase et al., 2000; Moreira et al., 1996; van der Zwan et al., 2015) and typical (ultra)slow-spreading mid-ocean ridge features are recognized in the bathymetry, including axial volcanoes, overlapping spreading centers and second-order offsets (Augustin et al., 2016).

Magnetic stripes along the axial trough between latitudes 15.5°–17.5°N suggest that oceanic seafloor spreading have occurred in the last 5 Myr (Cochran, 1983; Hall, 1989; Issachar, Ebbing, & Dilixiati, 2022; Schettino et al., 2016). Nevertheless, the nature of the crust beneath the sedimentary cover in the main trough and coastal plains is a matter of debate. Some authors argue that low amplitude magnetic anomalies indicate oceanic accretion between the axial trough and the Precambrian Shield in the southern Red Sea, while others interpret those as highly intruded transitional crust (see Almalki et al., 2015 for review). In the northern Red Sea, the lack of magnetic stripes, the morphology of the bathymetry, together with seismic profiles and geochemistry of rock samples suggest that this part of the basin is still in the stage of continental breakup and that oceanic accretion, if any, only started at discrete locations (Cochran, 1983; Ligi et al., 2019). On the contrary, recent studies interpreted gravity lineament (Augustin et al., 2021), rock geochemistry (Follmann et al., 2021) and correlated pre-rift

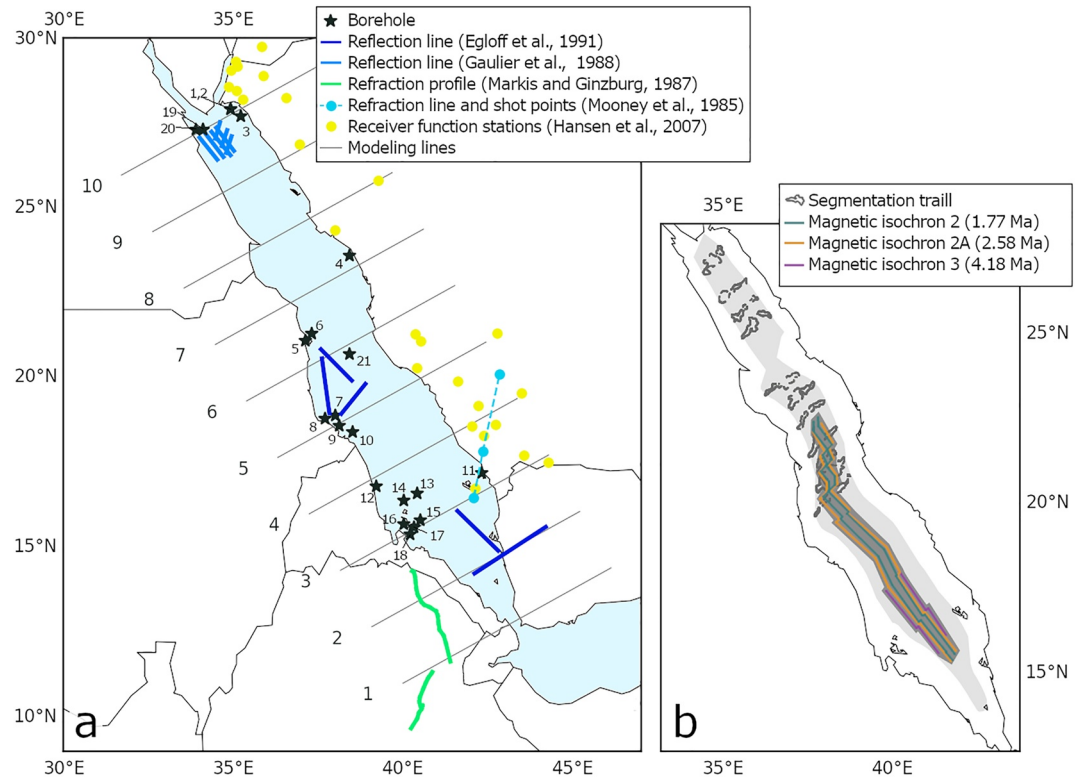


Figure 4. (a) Model-setup and geophysical constraints used to build the models. Geophysical data include seismic lines, receiver function stations and boreholes (Table 1). Black lines and associated numbers, indicate the location of the cross-sections defined in the modeling process. (b) segmentation trails (Augustin et al., 2021) and magnetic isochron (Schettino et al., 2016) in the Red Sea. The dark gray region denotes the area of oceanic crust in the *limited* option (Model 1 and Model 3). The light gray region denotes the area of oceanic crust in the *extended* option (Model 2 and Model 4).

rocks from the flanks of the Red Sea (Stern & Johnson, 2018) as evidence that oceanic crust is present within most of the basin. However, the lack of high-resolution seismic data and deep ocean drills makes it hard to prove the nature of the crust beneath the thick sedimentary cover.

2.2. Timing of Rifting and Volcanism

Several indicators, including the emplacement of dikes and subsidence related sedimentation suggest that during its initiation at Late Oligocene–Early Miocene (at ~23 Ma), rifting was present from Gulf of Suez

Table 1
Initial and Final Densities of the Lithospheric Models in kg·m⁻³

| Layer | Initial | | Final | | |
|------------------------------|------------|---------|---------|---------|---------|
| | All models | Model 1 | Model 2 | Model 3 | Model 4 |
| Sediments | 2,300 | 2,300 | 2,300 | 2,300 | 2,300 |
| Continental crust | 2,775 | 2,817 | 2,807 | 2,779 | 2,788 |
| Oceanic crust | 2,900 | 2,900 | 2,915 | 2,832 | 2,829 |
| Mantle lithosphere at 550°C | 3,330 | 3,330 | 3,330 | 3,330 | 3,330 |
| Mantle lithosphere at 900°C | 3,295 | 3,295 | 3,295 | 3,295 | 3,295 |
| Mantle lithosphere at 1100°C | 3,275 | 3,275 | 3,275 | 3,275 | 3,275 |
| Asthenosphere at 1300°C | 3,255 | 3,255 | 3,255 | 3,255 | 3,255 |
| Exhumed mantle | 3,000 | 3,000 | 3,000 | - | - |

down to the southern Red Sea (Morag et al., 2019; Plaziat et al., 1998; Stockli & Bosworth, 2018; Szymanski et al., 2016). The rift was preceded and accompanied by different phases of volcanism, mainly within the Arabian flanks (Aldaajani et al., 2021; Bosworth & Stockli, 2016). Nowadays, vast areas of elevated topography in Ethiopia and western Yemen are covered by flood basalts (Figure 1), which started to deposit ~8 Ma before of the rifting in the Red Sea (Prave et al., 2016) and are assumed to be associated with the arrival of the Afar plume head (Furman et al., 2006). Concurrently to the flood basalt volcanism in Ethiopia, the rifting in the Gulf of Aden started at the eastern parts (Almalki & Betts, 2021; Bosworth & Stockli, 2016; Manighetti et al., 1997), rapidly propagated westward and a mid ocean ridge formed along most of this basin (Fournier et al., 2010).

2.3. Deep Structure

Not much is known about the deep structure of the lithosphere beneath the Red Sea. The lack of modern active seismic data, ocean bottom seismometers and seismic networks on the western flanks limit the knowledge regarding the deep lithospheric configuration. Nevertheless, seismic tomography and receiver function studies have shed light on the lithospheric structure underneath the northern Red Sea and the Arabian shoulders (e.g., El Khrepy et al., 2021; Hansen et al., 2007; Mai et al., 2019; Yao et al., 2017). For instance, the source of the Cenozoic volcanism in Arabia has been attributed to a lateral heat flow from the Afar plume area, rather than from distinct deep mantle sources underneath the volcanic fields (Faccenna et al., 2013; Mai et al., 2019). Recent studies suggest a thin and hot lithosphere beneath the western Arabian shield (Hansen et al., 2008; Yao et al., 2017). In the northern Red Sea, the upwelling asthenosphere was imaged beneath the center of the basin, which deviates westward in the southern parts of the northern Red Sea (El Khrepy et al., 2021).

Rayleigh-wave tomography models using data from a dense seismic network in Afar triangle revealed low seismic velocity patterns associated with melt production, down to depths of 100 km (Gallacher et al., 2016). Segmented anomalies observed below the Afar triangle are connected to the Main Ethiopian Rift and to the Gulf of Aden, suggesting that mantle segmentation beneath the oceanic rifts initiated early during continental rifting (Gallacher et al., 2019).

2.4. Rifting Models for the Red Sea

Early works already proposed that a divergent convective flow in the asthenosphere derived the extension along the Red Sea, which resulted in a thinned continental lithosphere during the initial stages of the rifting (Lowell & Geni, 1972). Other models proposed that a short initial stage of mechanical thinning of the crust was followed by a long stage of magmatic expansion, which resulted in an extremely thin continental lithosphere at the central-southern Red Sea and the formation of broad shelves (Bohannon & Eittreim, 1991). In contrast, other works suggested that a diffuse extension resulted in a significant thinning of the continental crust, while the lithospheric mantle was exhumed and thickened before breakup was achieved (Cochran, 1983). Later models even proposed the existence of exhumed mantle rocks along wide areas in the basin, which was achieved by the activity of low-angle detachment faults that reach the lower lithosphere (Voggenreiter et al., 1988). In spite of many years of debates, these different suggestions were never settled, mainly because of the lack of reliable seismic data that can image the deep lithospheric structure.

3. Data and Methods

In order to distinguish between Type I and Type II margins, we examine the gravity response of four end-member models of lithospheric configurations, and evaluate their misfit with respect to the observed gravity anomalies in the Red Sea and in the African-Arabian flanks. Therefore, the deep structure of the rift, down to depths of 140 km is the main focus, and resolving fine details in the crystalline crust and sedimentary cover is not within the scope of this study. The four end-member models (Figure 2) were designed to test different hypotheses regarding margin types and the distribution of the oceanic crust together, as described in the next subsections.

3.1. Gravity Data Set

The 3D models were fitted to the Bouguer gravity anomalies which was derived from the XGM2019e data set (Zingerle et al., 2020). The XGM2019e is a global gravity field model combining satellite and terrestrial gravity measurements with a spatial resolution of ~25 km in the onshore domains and of ~4 km in the offshore domain.

For the aim of the study, we obtained the XGM2019e in a spatial resolution of 0.2° (~ 20 km) using ICGEM (Ince et al., 2019). Further, a simple Bouguer correction (Δg_B) was calculated using the conventional term:

$$\Delta g_B = 2\pi\rho GH, \quad (1)$$

where ρ is the density, G is the gravitational constant and H is the elevation. For onshore domains we used the common value of $\rho = 2,670 \text{ kg}\cdot\text{m}^{-3}$. For the offshore domains we used an infill density of $1,175 \text{ kg}\cdot\text{m}^{-3}$, which is the difference between the sea water density of $1,025 \text{ kg}\cdot\text{m}^{-3}$ and the offshore sediments density of $2,200 \text{ kg}\cdot\text{m}^{-3}$. These values are used to avoid large density contrast between water and sediments in the modeling process, and is a standard method used for offshore modeling (e.g., Haase & Ebbing, 2013). Elevations were derived from the Gebco compilation (GEBCO Compilation Group, 2021) (Figure 3a). The next step was to subtract this correction from the XGM2019e free-air anomalies (Figure 3b), obtaining the Bouguer gravity anomalies used in this study (Figure 3c).

3.2. Available Geophysical Data

3.2.1. Borehole Data

To estimate the thickness of sediments in the offshore domain we used data from 21 wells, drilled between the early 50's to the early 90's (Almalki et al., 2015; Izzeldin, 1987) (Table 2 and Figure 4a). Eleven wells reached the basement rocks and thus provide a direct observation of the sedimentary thickness, while the others only provide minimum values. Most of the wells were drilled close to the shoreline and suggest a maximum sediment thicknesses of ~ 4 km.

3.2.2. Seismic Observations

To better constrain sediment and crustal thicknesses in the study area, we used seismic data from five different experiments (Figure 4a). A survey from the northern Red Sea (Gaulier et al., 1988) suggests sedimentary sequences of ~ 6 km thick offshore Egypt, underlain by eastward dipping normal faults and an overall crustal thickness of ~ 13 km. Three reflection lines offshore Sudan (Egloff et al., 1991) indicate ~ 6 km sedimentary thickness in the coastal plains and a crustal thickness of ~ 15 km. The sedimentary thickness is significantly thins toward the axis of the Red Sea and a Moho shallowing (~ 7 km) is marked at ~ 100 km from the shore line. Two profiles offshore northern Yemen (Egloff et al., 1991; blue lines in Figure 4a) suggest a sediment thickness of ~ 4 km and Moho depths of ~ 12 km. A stepwise Moho topography thickens the crust up to 35 km on the onshore Yemen (blue line in Figure 4a). Complementary to borehole and seismic data, we used the GlobSed global compilation (Straume et al., 2019) to estimate sediment thickness in the entire offshore region (Figure S1a in Supporting Information S1).

Interpretation of a 1,000 km long seismic refraction profile in the southwestern Arabian flanks, collected in 1978, suggests ~ 40 km thick crust beneath the Arabian Shield that rapidly thins to less than 10 km offshore (Mooney et al., 1985). Seismic refraction lines in the Afar triangle, collected in the early 70's and re-interpreted by Makris and Ginzburg (1987) indicate thinned crust in northern Afar with Moho depths of ~ 15 km, and lack of crustal thinning in southern Afar with Moho depths of ~ 25 km. Notwithstanding the importance of these surveys, the interpretations are quite controversial due to the low quality of the data (in comparison to modern surveys) and the masking effect of the thick salt layers within the sediments in the offshore regions (e.g., Cochran, 2005).

In addition to active seismics, recent receiver function studies from Saudi Arabian stations indicate ~ 35 – 40 km thick crust beneath the Arabian shield and a rapid thinning with the proximity to the Red Sea (Hansen et al., 2007). These observations also provide information regarding lithospheric thickness, suggesting an LAB (Lithosphere Asthenosphere Boundary) depth of ~ 90 – 110 km beneath the Arabian shield (Hansen et al., 2007; Park et al., 2008), although a recent seismic tomography suggests the lithosphere might be thinner in the western parts of the shield (Yao et al., 2017). In the northern Red Sea, the recent tomographic model of El Khrepy et al. (2021) shows high-velocity anomalies coinciding with the Red Sea basin and a narrow low-velocity anomaly centered beneath the rift axis, interpreted as a transition of the lithospheric extension from continental rifting to oceanic spreading. In the central southern regions of the basin, the diluted seismic network in the western flanks hampers the accuracy of seismic tomography models.

3.2.3. Global Compilations

Several global compilations that infer the Moho topography in the study area are available (e.g., Afonso et al., 2019; Fulla et al., 2021; Reguzzoni & Sampietro, 2015; Szwillus et al., 2019). For the initial model set-up, we used data from Szwillus et al. (2019) (alongside the available seismic lines described above) as they provide a fully transparent workflow and do not rely on a priori geological assumptions. In later stages of the study, we compared our results to

other compilations which are based on gravity data. For the initial LAB topography we relied on the LithoRef global model (Afonso et al., 2019), which integrates different types of satellite gravity measurements (gravity anomalies, geoid height and satellite-derived gravity gradients), as well as on receiver function data from Hansen et al. (2007).

3.3. Models Set-Up

The end-member models were set-up in an area including the entire Red Sea, plus ~200 km from each of the African and Arabian flanks, and range between 0 and 140 km depth. The initial model included four horizons: sediments, top of crystalline crust, Moho and LAB (Figure S1 in Supporting Information S1). In particular, as the Moho and LAB data sets are based on globally available geophysical data, they generally lack the resolution required for the current study. Further, to simulate the four end-member types of rifted margins, we modified the Moho and LAB geometries below the rift area. The four end-member models consist of six layers: sediments, continental crust, oceanic crust, lithospheric mantle, exhumed mantle (in models 1 and 2) and asthenosphere. We assigned a starting density values based on representative lithologies for each layer (Table 1). As there is not enough available data to account for specific density variations in the entire basin, we assigned the common average density values to each layer of 2,300 kg·m⁻³ for the sediments, and 2,775 kg·m⁻³ and 2,900 kg·m⁻³ for the continental and the oceanic crust, respectively. For the upper mantle, we assigned an average value of 3,330 kg·m⁻³ (Mooney & Kaban, 2010; Poudjom Djomani et al., 2001) and added a vertical density gradient considering four steps of temperatures at 500, 900, 1100 and 1300°C, aiming to simulate an heterogeneous mantle configuration (Fischer et al., 2010). The effect of the temperature on the density, assuming a constant composition, was calculated as (e.g., Chappell & Kusznir, 2008):

$$\Delta\rho = -\alpha\rho\Delta T, \quad (2)$$

where α is the thermal expansion coefficient, which we assumed as $3.28 \times 10^{-5} \text{ K}^{-1}$, typical for young plates and oceanic domains (Afonso et al., 2005). For the exhumed mantle (in models 1 and 2), a constant density of 3,000 kg·m⁻³ was assigned, considering the effect of density reduction due to serpentinization (Bonnemains et al., 2016; Hyndman & Peacock, 2003; Liu et al., 2021; Rüpke et al., 2013; Toft et al., 1990). Table 1 summarizes the starting densities assigned to the different layers.

3.4. Modeling Approach

We implemented an interactive forward modeling approach to fit each of the 3D lithospheric density structures to the measured gravity anomalies, using the software package IGMAS+ (Götze & Lahmeyer, 1988; Schmidt et al., 2011, 2020). To explore the gravity response of the models, we defined 10 cross-sections perpendicular to the rift axis, 200 km apart from each other (Figure 4a).

Figure 5 presents the forward modeling approach followed in this study. First, we calculated the gravity response of the initial model, focusing on the gravity residuals, that is, subtracting the calculated from the observed gravity at each grid point. In the next step, we interactively modified the Moho and LAB geometries according to the end-member type of margins, attempting to minimize the residuals at each cross-section, while at the same time avoiding large deviations from the constraints. For example, we did not change the initial geometries of the sedimentary layer, nor the lateral extent of the oceanic crust. Additionally, we restricted the thickness of the oceanic crust to a maximum of 10 km, as considered realistic in other oceanic basins (Perfit, 2001). After modifying the geometries of the Moho and LAB, we optimized the densities of the continental and oceanic crystalline crusts, using the minimum mean square error linear inversion, available in IGMAS+ (Haase, 2008). These steps were repeated till the best fit to the observed gravity was achieved. The initial and final densities are presented in Table 1, and the initial and final model horizons are presented in Figures S1 and S2 in Supporting Information S1.

Last but not least, to validate whether our modeling approach is sensitive to heterogeneities in the upper mantle, we performed a sensitivity test to the end-member models. This was done by analyzing the gravity response to lateral density heterogeneities at depths below 40 km (e.g., Fullea et al., 2021). For details regarding the technical aspects of this test see the Supporting Information S1. The four end-member structural and density models tested in this research are available in the data repository Issachar, Gómez-García, and Ebbing (2022).

4. Results

Figure 6 shows the lithospheric configuration and the associated gravity response for each end-member model along cross-section #5 (see Figure 4a for location). The models fit the observed gravity along the rift shoulders

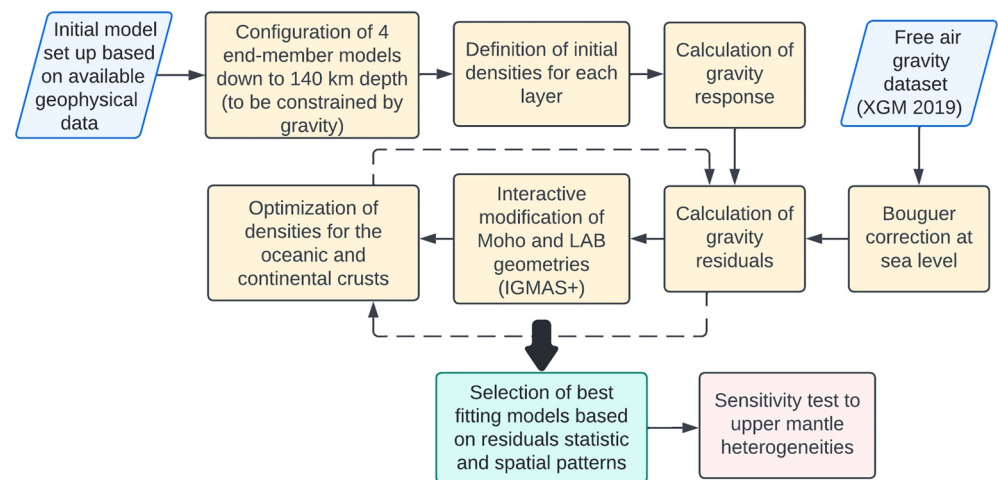


Figure 5. Methodological scheme for the modeling process.

and the coastal plains; however, there are significant misfits within the basin in some of the models. Models 1, 2 and 4 fail to fit the narrow anomaly above the axial trough in the center of the basin. In these models, both the high-density oceanic crust and exhumed mantle have a high gravity response. Model 3, on the contrary, fits the observed gravity within the basin more accurately (Figure 6c). Here, the low gravity signal above the coastal plains implies a ~15 km thick rifted continental crust, while the pronounced anomaly above the axial trough is related to a high-density oceanic crust and a shallow asthenosphere (Table 2).

Figure 7 depicts the gravity residuals of the four tested models. Model 3 has the lowest residual values for the entire Red Sea, with a standard deviation of ± 17.6 mGal. The residuals histogram is less skewed and centered around zero mGal (Figures 7c and 7e).

In the central-southern regions of the basin, south of latitude 23°N (approximately corresponding to cross-section #7), Model 3 is clearly preferable, as the residuals are minimized (Figure 7) and the intra-basin anomalies are well fitted (Figure 6c). This model is characterized by ultrawide margins, which extent along most of the width of the rift (Figure 8), and includes crustal thinning in the Afar region. In the other models, there are two basin parallel negative residuals along the middle of the basin, more prominent in models 2 and 4, which have an extended oceanic crust distribution (Figures 6 and 7). It is worth noting that in all models, we obtain persistent positive residuals along the shoreline of the southern Arabian flank.

In the region north of latitude 23°N, all models have comparable low residuals (Figure 7). Nevertheless, in the offshore area, Model 1 (Figure 9) shows a very good correlation to the recent body wave tomography model of El Khrepy et al. (2021) (Figure 10). Particularly, the regions of asthenosphere upwelling below the middle of the basin spatially correlate with the low velocity zones in the tomographic model. Hence, we consider Model 1 as preferable in the northern regions of the Red Sea. This end-member model is characterized by an exhumed mantle lithosphere and a narrow asthenosphere upwelling below the center of the basin (Figure 9).

The sensitivity test indicates that end-member models are sensitive to lateral changes in the upper mantle. A significant gravity effect of up to 25% is observed by introducing lateral heterogeneities of ~1% (Figures S3a and S3b in Supporting Information S1), suggesting that our modeling approach is capable to reflect deep lithospheric structures, for example, the LAB geometry beneath the rift shoulders.

5. Discussion

5.1. Lithospheric Structure in the Red Sea

5.1.1. The Central-Southern Red Sea

Our modeling suggests that in the central-southern parts of the Red Sea, south of latitude 23°N, a model of Type II margin architecture better explains the Bouguer anomalies (Model 3, Figure 8). In this region, the anomalies have a positive peak of more than 150 mGal above the axial trough, which symmetrically drops to -25 mGal toward the coasts (Figure 3c). Considering that the axial trough is the deepest area in the Red Sea, the

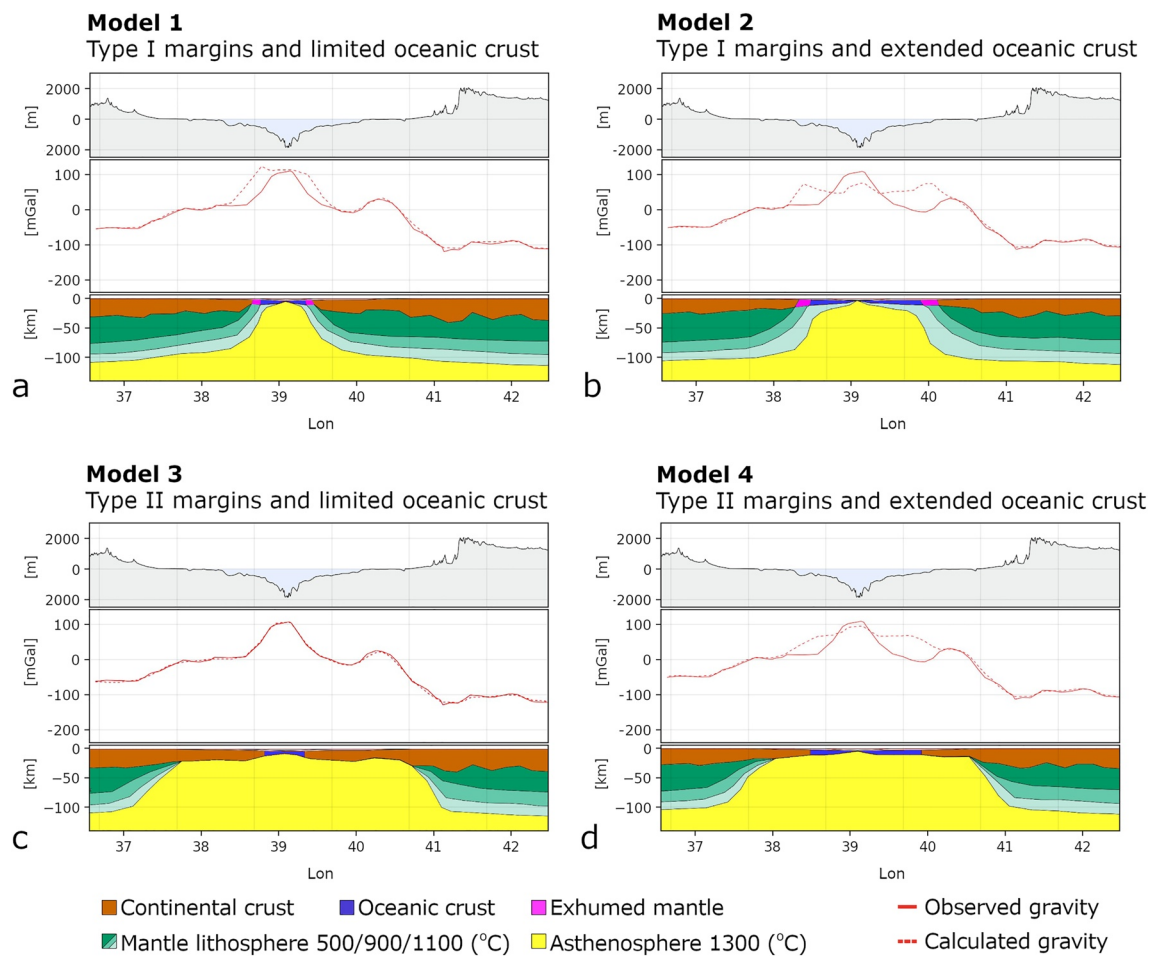


Figure 6. Cross-sections and their corresponding gravity response for each end-member model. Profiles along cross-section #5 showing from bottom to top: lithospheric configuration, associated gravity values and surface elevation. Refer to Table 1 for selected densities.

pronounced Bouguer gravity high observed over the axial trough (Figure 6) indicates a mass surplus at depth. Thus, a lithospheric model, which considers exhumed mantle rocks close to the rift flanks, like in Model 1 and Model 2 (Type I margin), fails to fit the gravity trend (Figures 6a and 6b). By significantly reducing the density of the exhumed mantle rocks in Model 1 and Model 2, it is possible to fit Type I margins to the observed gravity; however, it implies a complete serpentinization (density of $2,500 \text{ kg}\cdot\text{m}^{-3}$; Hyndman & Peacock, 2003) down to depths of $\sim 15 \text{ km}$, which is unrealistic (e.g., Liu et al., 2021). Moreover, a significant mantle serpentinization in rifts is expected to occur mainly for thin sedimentary cover and high stretching factors (Rüpke et al., 2013), which is not the case in the southern Red Sea. Furthermore, a model that considers an extended distribution of oceanic crust in the southern regions, that is, thin and dense crust beneath the coastal plains like in Model 4, also fails to fit the pronounced gravity high along the axis of the rift (Figure 6d). By allowing oceanic crustal thicknesses of $\sim 15 \text{ km}$ beneath the coastal plains in Model 4, it is possible to fit also the extended oceanic crust distribution; however, an oceanic crust of such thickness has not been reported along other slow-spreading ridges (Klingelhöfer et al., 2000). For example, in the mid-Atlantic (35°N), maximal crustal thickness of 8 km was observed in seismic profiles, $\sim 50 \text{ km}$ from the current ridge (Carbotte, 2005). Therefore, we find no reason to suppose a $\sim 15 \text{ km}$ thick oceanic crust in the Red Sea. Thus, Model 3 that is characterized by ultrawide margins, the removal of mantle lithosphere and a broad asthenosphere upwelling (Type II; Figure 8), is the only option which realistically resolves the Bouguer gravity anomalies in the central-southern Red Sea.

5.1.2. The Northern Red Sea

In the northern Red Sea, the characteristics of the gravity field are different than those of the central-southern region. North of latitude 23°N , the Bouguer gravity anomalies are moderately positive within the entire region, with some

Table 2
Borehole Data Used in This Study

| Borehole name | Location (Lat/Lon) | Sedimentary thickness (m) | Bottom rock and lithology remarks | Reference |
|----------------------------------|--------------------|---------------------------|--|-----------------------|
| Bargan-1 (1) ^a | 27.9/34.9 | 2,900 | Granite | Izzeldin (1987) |
| Bargan-2 (2) ^a | 27.9/34.9 | 2,786 | Granite | Izzeldin (1987) |
| Yuba-1 (3) ^a | 27.7/35.2 | 2,271 | Granite | Izzeldin (1987) |
| Badr-1 (4) | 23.6/38.4 | >3,348 | Shale | Izzeldin (1987) |
| Dungunab-1 (5) ^a | 21.1/37.1 | 1,615 | Volcanic tuff overlying granite basement. Basalt sill at 1,094–1,118 m | Izzeldin (1987) |
| Abu shagara-1 (6) ^a | 21.3/37.3 | 2,000 | Igneous at 2,000 m | Izzeldin (1987) |
| Suakin-1 (7) | 18.9/38 | >2,745 | Sandstone | Izzeldin (1987) |
| Durwara-2 (8) ^a | 18.8/37.7 | 4,152 | Basalt | Izzeldin (1987) |
| Bashayr (9) | 18.6/38.1 | >2,787 | Anhydrite | Izzeldin (1987) |
| South suakin-1 (10) | 18.4/38.5 | >3,712 | Limestone, silt stone with Lignite | Izzeldin (1987) |
| Mansiyah-1 (11) | 17.2/42.3 | >3,939 | Sandstone and shale. Volcanic interbeds between 1,981 and 2,195 m | Izzeldin (1987) |
| C-1 (12) | 16.8/39.2 | >3,010 | Sandstone | Izzeldin (1987) |
| B-1 (13) ^a | 16.6/40.4 | 1,323 | Basalt interbedding | Izzeldin (1987) |
| Amber-1 (14) ^a | 16.4/40 | 3,557 | Metamorphics | Izzeldin (1987) |
| Dunishub-1 (15) | 15.8/40.5 | >3,667 | Salt and shale | Izzeldin (1987) |
| Suri-7 (16) | 15.7/40 | >2,553 | Salt and anhydrite | Izzeldin (1987) |
| Adal-2 (17) | 15.6/40.3 | >2,475 | Salt anhydrite and shale | Izzeldin (1987) |
| Secca Fawn-1 (18) | 15.4/40.2 | >3,363 | Shale dolomite and anhydrite. Penetrate several volcanic horizons | Izzeldin (1987) |
| Hareed South 3 (19) ^a | 27.3/34.1 | 1,683 | Granite | Almalki et al. (2015) |
| Abu Shiban-2 (20) ^a | 27.3/33.9 | 2,836 | Granite | Almalki et al. (2015) |
| 227 (21) ^a | 20.7/38.4 | 359 | Salt, Basalt (bottom) | Almalki et al. (2015) |

Note. See Figure 4 for well locations.

^aWell that reached basement. Numbers after the borehole name indicate the location of the well in Figure 4a.

isolated peaks of up to 85 mGal (Figure 3c). In this region, all four models could fit the observed gravity with relatively low residuals (Figure 7). In Model 2 and Model 4, which have an extended oceanic crust distribution, we obtained similar Moho depths to those interpreted by Gaulier et al. (1988) from seismic lines, but we had large disagreements with Hansen et al. (2007) who inferred ~30 km of crustal thickness close to the Arabian shore from receiver function data. Taking this into account, together with the very good agreement of Model 1 to the recent tomography model of El Khrepy et al. (2021) (Figure 10), we suggest that the limited oceanic crust option is more realistic for the northern Red Sea. Although segmentation trails were inferred from the vertical gravity gradient data to support an extended oceanic crust distribution in this area (Augustin et al., 2021), previous gravity interpretations are also in disagreement regarding such lithospheric setting (e.g., Almalki et al., 2016; Saada et al., 2021; Saleh et al., 2006).

Changes of lithospheric structure along the axis of the Red Sea have also been inferred from earthquake hypocentral analyses (e.g., El-Isa, 2015; Mitchell & Stewart, 2018). The northern region of the rift shows a decrease in seismicity rates compared to the central-southern regions, with an abrupt drop in the occurrence of earthquakes at a transition zone around 21° to 23°N. Several hypotheses could explain the modest seismicity of the northern basin, including: the presence of a weak serpentinized upper mantle (Mitchell & Sofianos, 2018), which was also inferred from deep Curie depths (Ravat et al., 2011); the increase in lithospheric temperatures due to the thermal blanketing effect caused by the thick sedimentary units in this region; and lastly, the decrease of effective stress associated to the high fluid pressure underneath the thick evaporite sequence (Mitchell & Stewart, 2018). Although our modeling result may support the presence of a serpentinized upper mantle, suggesting an exhumed mantle lithosphere and Type I margins in the northern Red Sea (Figure 9), the temperatures at which serpentinized material is stable (<400°C) might imply proper conditions for seismogenesis, which is not currently observed in the seismic records.

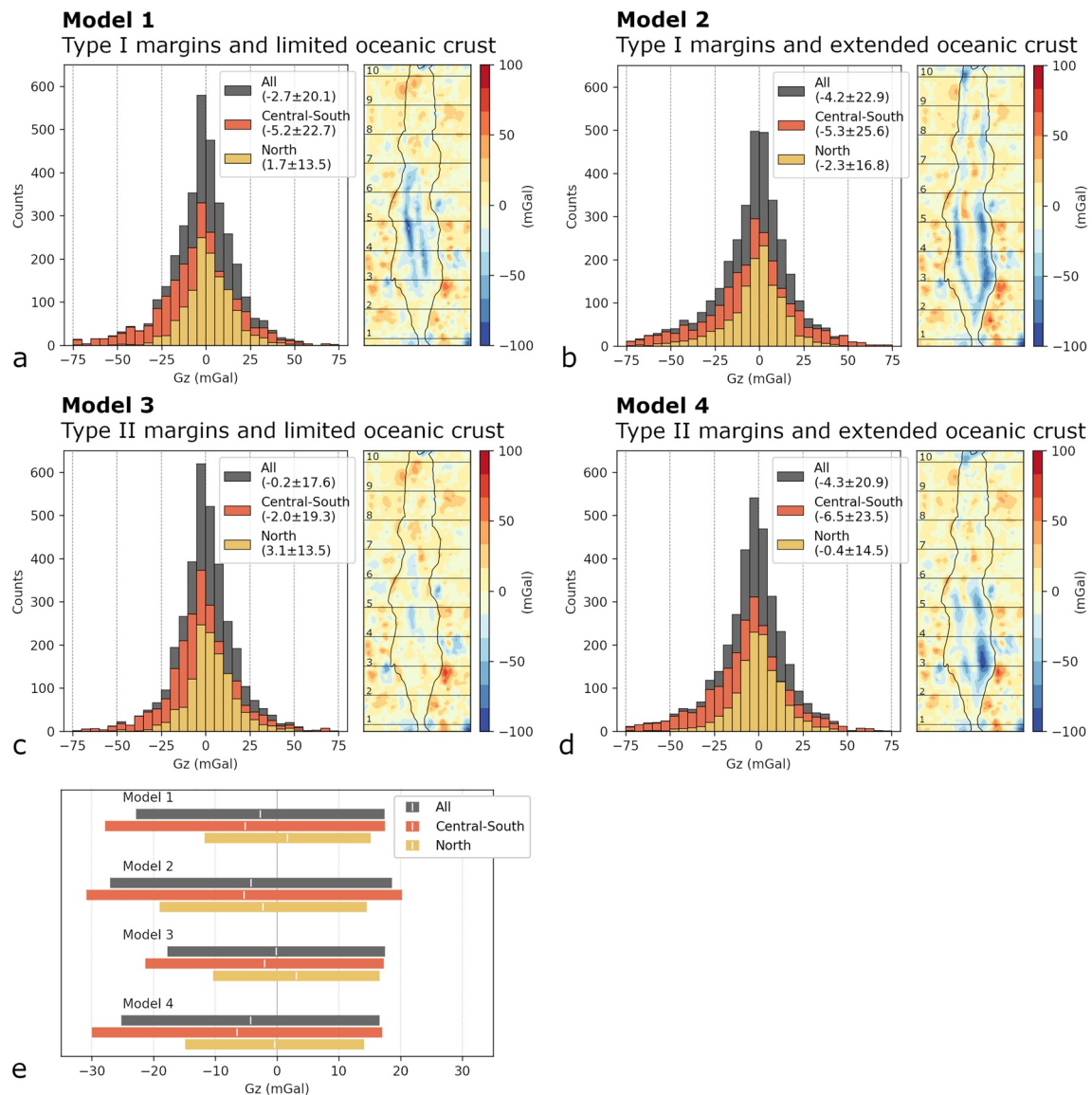


Figure 7. (a–d) Residual maps and histograms of the four end-member models. The residuals are defined as observed minus calculated gravity fields. Black solid lines and associated numbers on the maps indicate the location of the cross-sections defined in the modeling process. The gray histograms represent the residuals of the entire study area, the orange correspond to the areas between cross-section #1 and cross-section #7, and the yellow ones to the regions north of cross-section #7. (e) Standard deviations of the residuals of the four models. White bars indicate average residual value.

5.1.3. Magmatic Underplating

Another distinct feature of the gravity field is a positive anomaly trend of ~ 30 mGal along the Arabian coast in the central-southern regions (dashed polygon in Figures 3b and 3c). This ~ 700 km elongated feature also appears in the free-air anomalies but does not show a topographical correlation. Although this anomaly could be compensated by reducing the crustal thickness, a likely explanation in line with the seismic constraints on crustal thickness would be a high-density crustal feature. Large magmatic intrusions, such as magmatic underplating or mafic intrusions (sills and dikes) are frequently observed along magma-rich margins (Geoffroy, 2005). The gravity modeling suggests that this anomaly could be correlated to a high-density body at the base of the crust (Figure 11). By introducing a body with a density of $2,900 \text{ kg}\cdot\text{m}^{-3}$ beneath the Arabian shoreline, Model 3 fits the observed gravity with no additional crustal thinning. This body may imply the presence of underplated magma in the lower crust, which is often characterized by high seismic velocities (Kelemen & Holbrook, 1995; Sapin et al., 2021). Indeed, a high velocity zone was observed beneath the western Arabian shield, overlaid by a low-velocity zone in the upper mantle (Yao et al., 2017). Moreover,

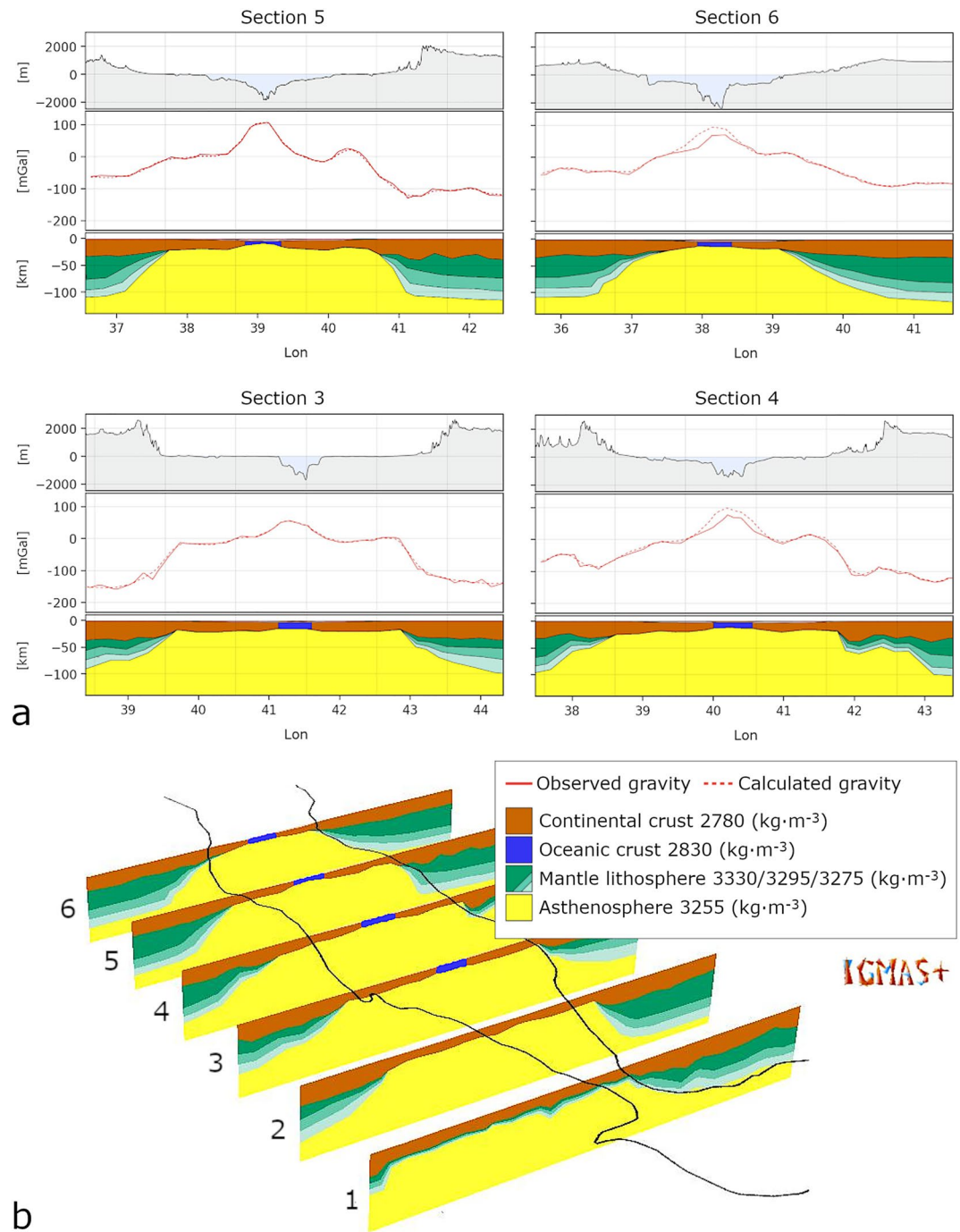


Figure 8. Model 3 (Type II margins and limited oceanic crust) - Best fitting model for the central-southern regions of the Red Sea. (a) Profiles showing from bottom to top: lithosphere geometry, associated gravity values and surface elevation. (b) Three-dimensional representation of the model.

the proposed underplated body fits the general pattern of magmatism in this region, including vast regions of exposed magmatic fields and basaltic dike swarms of Late Oligocene and younger along the Arabian flanks (Figure 11a).

5.2. Influence of the Mantle Plume

The results of the gravity modeling show a contrasting rift architecture in the central-southern regions and in the northern region of the Red Sea. In the central-southern regions (south of 23°N), the rift architecture is characterized

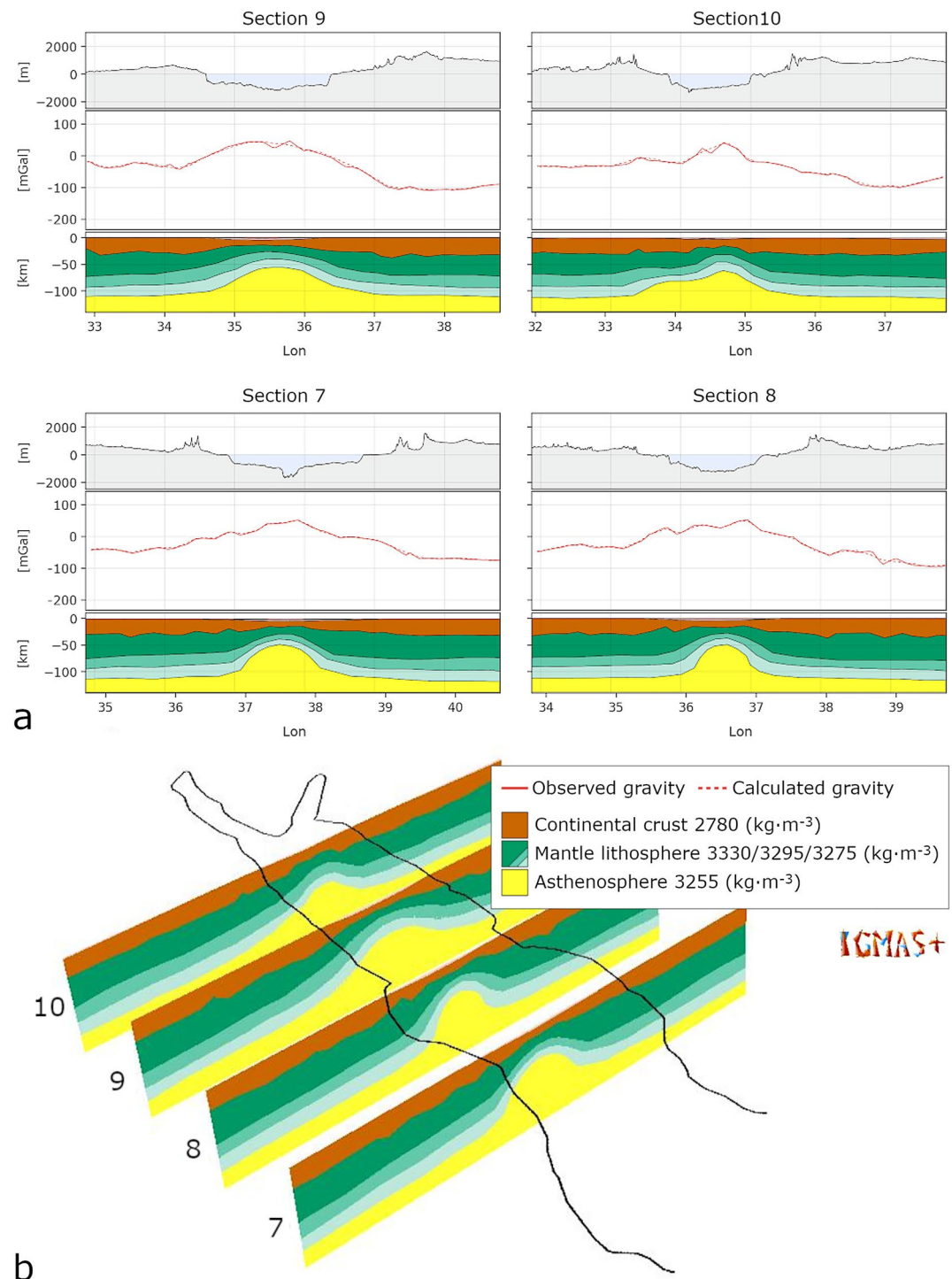


Figure 9. Model 1 (Type I margins and limited oceanic crust)—Suggested model for the northern region of the Red Sea. (a) Profiles showing from bottom to top: lithosphere geometry, associated gravity values and surface elevation. (b) Three-dimensional representation of the model.

by ultrawide margins (Type II), in which the mantle lithosphere is absent below a thinned continental crust (Figure 8). Such an architecture implies the breakup of the mantle lithosphere during earlier stages of rifting, while the upper crust experiences a protracted extension. This architecture is observed along conjugate margins worldwide, for example, Brazil-Angola conjugates (Moulin et al., 2005; Péron-Pinvidic et al., 2017; Unternehr et al., 2010). Numerical studies point the rheology of the lower crust as a prime factor allowing the development of this rift type, where

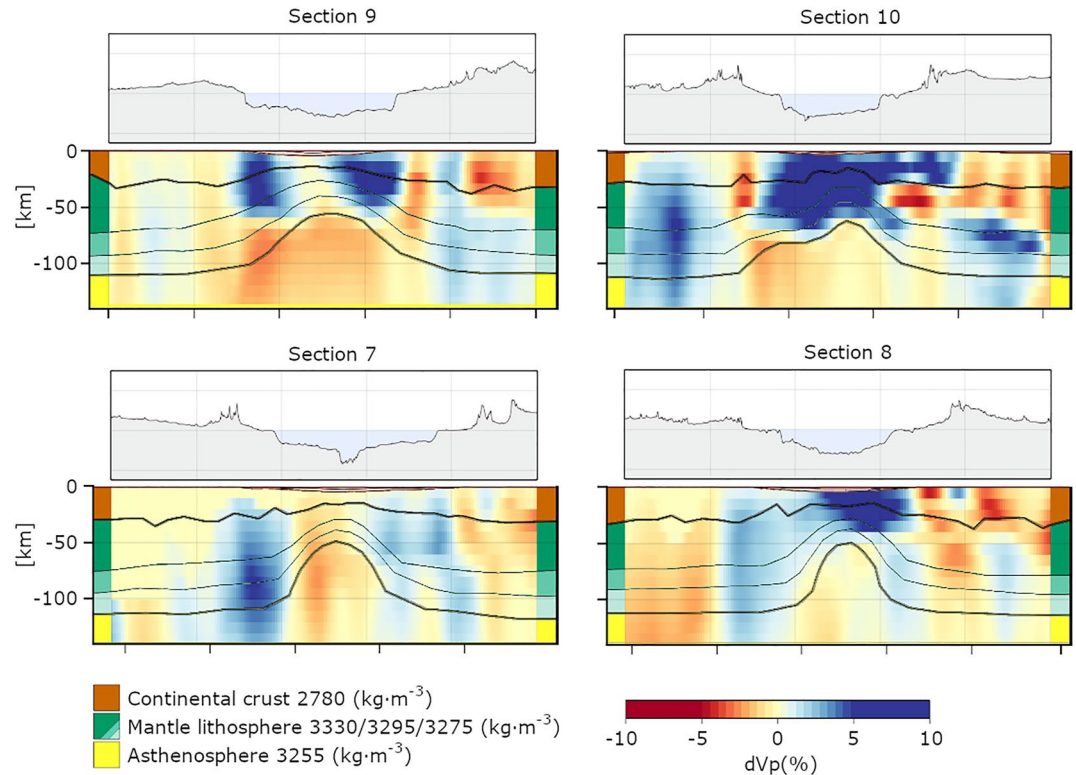


Figure 10. Profiles showing the structural and density distribution of Model 1 and their spatial correlation with the seismic tomography model of El Khrepy et al. (2021), as regions of asthenosphere upwelling below the basin correlate with low velocity zones. We suggest this model is representative of the rift architecture in the northern Red Sea (see Figure 3 for locations). The gray lines indicate the lithosphere geometries of Model 1, where the thick lines are the Moho (top) and the LAB (bottom).

a weak lower crust acts as ductile decoupling layer, allowing large timespan differences between the breakup of the mantle lithosphere and the breakup of the upper crust (Brune et al., 2017; Huisman & Beaumont, 2011, 2014).

We propose that the proximity to the Afar plume could explain the development of this rift architecture in the central-southern Red Sea, by a reduction of the strength of the lower crust after the arrival of hot mantle material. The recent seismic tomographic model of Celli et al. (2020) shows low S-wave seismic velocities in the upper mantle parallel to the Red Sea, which are generally correlate with onshore volcanism (Figure 12a). A profile along the axis of the Red Sea (Figure 12b) shows that the central-southern region is characterized by low seismic velocities up to depths of 30 km, in contrast to the northern region, where the S-wave velocities are higher. Considering that the S-waves are highly sensitive to temperature, such trends indicate that the upper mantle in the south is hotter than in the north.

Figure 12c presents the +25% temperature contour (δT) down to depths of 100 km, obtained from the thermal model of Fullea et al. (2021). Here, it is possible to observe a spatial correlation between the temperature field and the suggested margin types, with the Type II region associated with the hotter lithosphere. The high temperature gradients seem to have a long influence of more than 1,000 km from the present-day plume location. A long distance impact of a plume on a rift was also suggested for the north Atlantic by the propagation of hot material at the base of the lithosphere (Koptev et al., 2017). This mechanism could also explain the different architectures along the Red Sea, as suggested by our results. In fact, by introducing a weak lithospheric mantle along the central-southern regions, Molnar et al. (2020) managed to reproduce first order features of the rift, including the associated kinematics, the rapid south to north propagation and the associated topography. By this, they proposed that a weak zone in the lithospheric mantle affected the overall mechanical behavior of the rifting process.

The western Gulf of Aden also developed in a close proximity to the Afar plume, although this rift initiated from the Indian ocean on the east (Manighetti et al., 1997). In contrast to the central-southern Red Sea, the Gulf of Aden

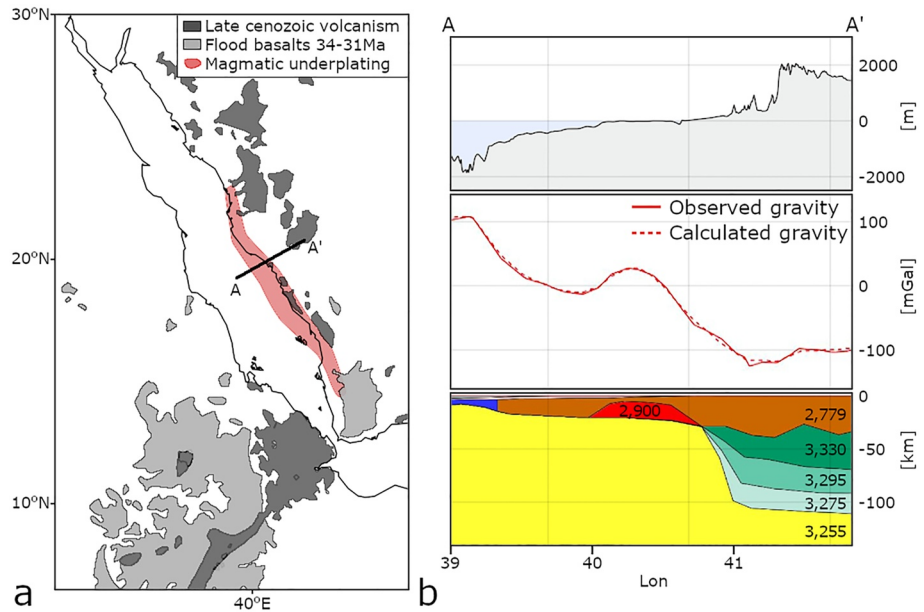


Figure 11. Suggested underplated magmatic body along the southern Arabian coast. (a) Gray polygons mark the mapped terrains of surface exposed Cenozoic volcanism (see Figure 1 for details). Red polygon denotes the modeled high-density body located at the base of the crust. (b) Profile along A–A' showing from bottom to top (Model 3): lithosphere geometry, associated gravity values and surface elevation. The model includes magmatic underplating (red), oceanic crust (blue) continental crust (brown), mantle lithosphere (green) and asthenosphere (yellow). Densities are specified in $\text{kg}\cdot\text{m}^{-3}$.

margins appear extremely short (e.g., Autin et al., 2010). Here, the basin deeps abruptly close to the shoreline (Figure 3a) and magnetic isochrones (Fournier et al., 2010) and seismic profiles (Gillard et al., 2021) suggest a nearly margin-to-margin seafloor spreading. Bellahsen et al. (2013) inferred that the thermal anomaly of the Afar plume may helped in the localization and the development of the rift-parallel faulting in the western Gulf of Aden. We suggest three main factors to explain the difference between the ultrawide architecture of the margins in the

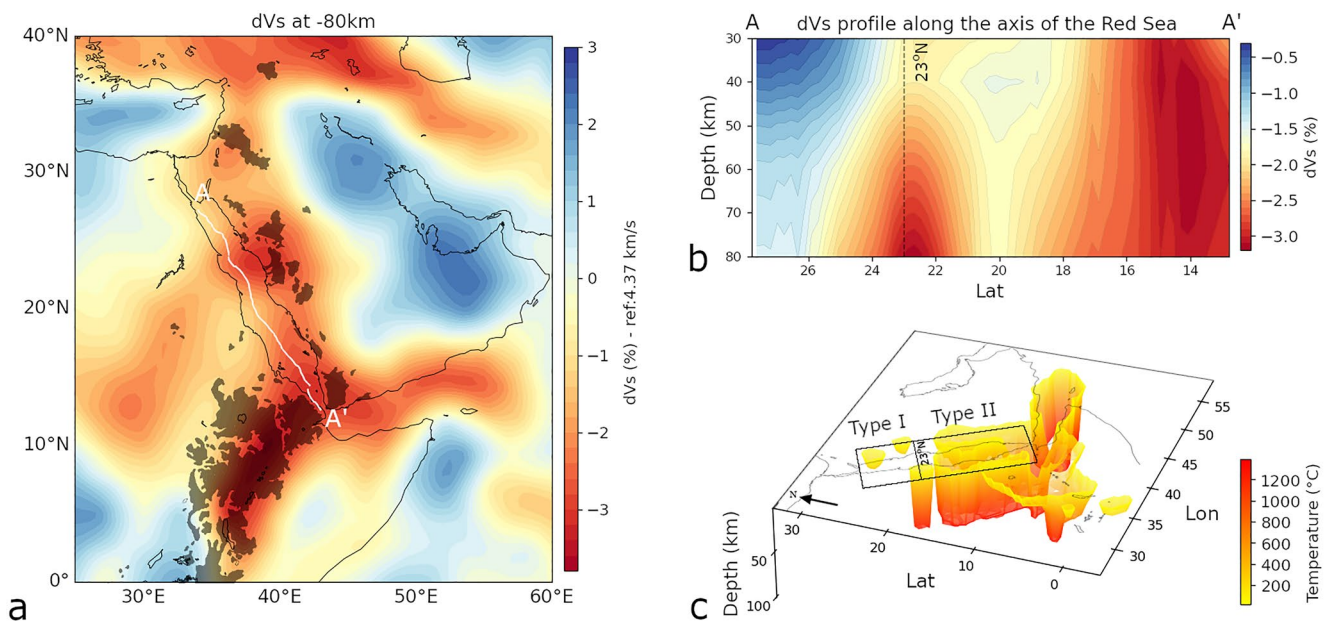


Figure 12. (a) Shear wave velocities at 80 km depth (after Celli et al., 2020). Black shades indicate Cenozoic volcanism exposures (see Figure 1 for more details). (b) Tomographic profile (A–A') along the Red Sea axis (after Celli et al., 2020). Dashed line demarks latitude 23°N. (c) Three-dimensional representation of the temperature field, calculated from WINTERC-G data (Fullea et al., 2021). The +25% δT contour is plotted between depths of 10 and 80 km. The view is looking from the west.

central-southern Red Sea and in the narrow margins in the western Gulf of Aden: (a) the timing of the rifting relative to the plume activity. Rifting in the Gulf of Aden began at early to mid-Oligocene (~31 Ma) (Bosworth et al., 2005), simultaneously to the deposition of flood basalts in Ethiopia (Prave et al., 2016), whereas, in the Red Sea the rifting initiated ~8 Myr later at Late Oligocene-Early Miocene (~23 Ma) (e.g., Stockli & Bosworth, 2018). This time span could result in a significant difference in the pre-rifting weakening of the lithosphere in the Red Sea versus the Gulf of Aden (e.g., François et al., 2018). (b) The thermal blanketing effect of the sedimentary cover. Contrary to the Gulf of Aden, which always had a wide and deep marine connection to the Indian ocean, the Red Sea had only an episodic narrow and shallow marine connection via the Gulf of Aden and/or the Mediterranean. This resulted in over 6 km of a syn-rift sedimentary column throughout the Red Sea basin, including massive evaporite sequences (Bosworth et al., 2005). The blanketing effect of sediments has shown to be significant in the thermal history of rifted margins (Clerc et al., 2016; Lagabrielle et al., 2016), and can highly vary from a margin to another, depending on the sediment thickness and its nature (Clerc et al., 2018). The thick and rich evaporitic sediments in the Red Sea probably increased the geothermal gradients, contributing to the weakening of the lithosphere (Theissen & Rüpke, 2010). (c) The rift kinematics and structural inheritance. Rifting in the Gulf of Aden is characterized by higher extension rates than in the Red Sea, especially during the early rifting stages (~22 vs. ~14 mm/yr; DeMets & Merkouriev, 2016). In addition, the Gulf of Aden opened in an orthogonal orientation to the pre-existing structures, which probably had a major influence on the development of the intra-rift structures compared to the plume-induced weakening of the lithosphere (Autin et al., 2013; Brune & Autin, 2013).

In summary, the close proximity of the Afar plume, together with the prolonged time span between the arrival of the plume and the rifting in the Red Sea, plus the aid of the thick sedimentary cover could contribute to the thermal weakening of the lithosphere and to the development of ultrawide margins in the southern-central Red Sea. In contrast, the lithospheric mantle in the northern Red Sea is colder and less affected by the plume-related thermal anomaly, as can be observed in the present-day thermal field (Figure 12c). Latitude 23°N demarks the transition zone between Type I and II margin architectures, suggesting a direct implication of the plume dynamics in the development of the Red Sea rifting styles.

6. Conclusions

We explored the lithospheric structure and the architecture of the rifted margins in the Red Sea by modeling the Bouguer gravity anomalies of four end-type rifting models. We adopted a 3D modeling approach in which we interactively modified the Moho and the LAB geometries along the entire Red Sea and the associated African and Arabian shoulders. Our main conclusions are:

1. An ultrawide margin architecture (Type II) fits the Bouguer gravity anomalies and the geophysical constraints in the central-southern regions, south of latitude 23°N. In this region, a thinned continental crust is underlain by a broad asthenosphere upwelling, implying an early breakup of the mantle lithosphere alongside a protracted extension of the upper crust. We speculate that this kind of architecture is the result of a lithospheric weakening due to the proximity to the Afar plume, an extensive syn-rift sedimentation, and a long-time span (~8 Myr) between the arrival of the plume and the initiation of rifting.
2. In the northern region of the Red Sea, north of latitude 23°N, the results suggest a rift architecture of an exhumed mantle lithosphere and a narrow asthenospheric upwelling (Type I).
3. A high-density body is present at the base of the crust along the southern Arabian coast, probably associated with magmatic underplating processes.

In order to better correlate the rift structure with the thermo-mechanical state of the lithosphere and the activity of the Afar plume, an integrated approach is required. This is particularly true given the tectonic setting of the Red Sea, because a thick sedimentary layer could overprint the mantle temperatures at shallow depths, affecting the final rheological behavior of the lithosphere.

Data Availability Statement

The IGMAS + models produced in this study are available at Issachar, Gómez-García, and Ebbing (2022).

The XGM2019e gravity data set is available at <http://icgem.gfz-potsdam.de/calgrid>.

The Gebco bathymetry and topography compilation is available at https://www.gebco.net/data_and_products/gridded_bathymetry_data/#global.

The GlobSed Version 3 is available at <https://ngdc.noaa.gov/mgg/sedthick/>.

The AF2019 3-D shear-wave model for Africa (Celli et al., 2020) is available at <https://ds.iris.edu/ds/products/emc-af2019/>.

The WINTERC-G global upper mantle thermochemical model (Fullea et al., 2021) is available at <https://zenodo.org/record/5771863#.Y6gmBHZBzfs>.

The tomographic inversion in the Red Sea area (El Khrepy et al., 2021) is available at <https://zenodo.org/record/4482096#.Y6gnPHZBzfs>.

The modeling process was performed using the software package IGMAS+ (Götte & Lahmeyer, 1988; Schmidt et al., 2011, 2020), available at <https://igmas.git-pages.gfz-potsdam.de/igmas-pages/>. Figures and maps were made with Matplotlib version 3.2.1, available under the Matplotlib license at <https://matplotlib.org>.

Acknowledgments

This work was supported by a Minerva Fellowship granted to R. I. We thank Hans-Jürgen Götte, Sabine Schmidt and the Basin Modelling group at the GFZ (German Research Centre for Geosciences) for providing the interactive gravity and magnetic modelling software IGMAS+. We wish to thank two anonymous reviewers for providing constructive comments that helped to improve the paper. Open Access funding enabled and organized by Projekt DEAL.

References

- Afonso, J. C., Ranalli, G., & Fernández, M. (2005). Thermal expansivity and elastic properties of the lithospheric mantle: Results from mineral physics of composites. *Physics of the Earth and Planetary Interiors*, 149(3–4), 279–306. <https://doi.org/10.1016/j.pepi.2004.10.003>
- Afonso, J. C., Salajegheh, F., Szwillus, W., Ebbing, J., & Gaina, C. (2019). A global reference model of the lithosphere and upper mantle from joint inversion and analysis of multiple data sets. *Geophysical Journal International*, 217(3), 1602–1628. <https://doi.org/10.1093/gji/ggz094>
- Aldajani, T. Z., Almalki, K. A., & Betts, P. G. (2021). Plume versus Slab-Pull: Example from the Arabian plate. *Frontiers of Earth Science*, 9, 494. <https://doi.org/10.3389/FEART.2021.700550>
- Almalki, K. A., & Betts, P. G. (2021). Gulf of Aden spreading does not conform to triple-junction formation. *Geology*, 49(6), 672–676. <https://doi.org/10.1130/G48529.1>
- Almalki, K. A., Betts, P. G., & Ailleres, L. (2015). The Red Sea – 50 years of geological and geophysical research. *Earth-Science Reviews*, 147, 109–140. <https://doi.org/10.1016/j.earscirev.2015.05.002>
- Almalki, K. A., Betts, P. G., & Ailleres, L. (2016). Incipient seafloor spreading segments: Insights from the Red Sea. *Geophysical Research Letters*, 43(6), 2709–2715. <https://doi.org/10.1002/2016GL068069>
- Altherr, R., Henjes-Kunst, F., & Baumann, A. (1990). Asthenosphere versus lithosphere as possible sources for basaltic magmas erupted during formation of the Red Sea: Constraints from Sr, Pb and Nd isotopes. *Earth and Planetary Science Letters*, 96(3–4), 269–286. [https://doi.org/10.1016/0012-821X\(90\)90007-K](https://doi.org/10.1016/0012-821X(90)90007-K)
- Augustin, N., van der Zwan, F. M., Devey, C. W., & Brandsdóttir, B. (2021). 13 million years of seafloor spreading throughout the Red Sea Basin. *Nature Communications*, 12, 1–10. <https://doi.org/10.1038/s41467-021-22586-2>
- Augustin, N., van der Zwan, F. M., Devey, C. W., Ligi, M., Kwasnitschka, T., Feldens, P., et al. (2016). Geomorphology of the central Red Sea Rift: Determining spreading processes. *Geomorphology*, 274, 162–179. <https://doi.org/10.1016/j.geomorph.2016.08.028>
- Autin, J., Bellahsen, N., Leroy, S., Husson, L., Beslier, M. O., & d'Acremont, E. (2013). The role of structural inheritance in oblique rifting: Insights from analogue models and application to the Gulf of Aden. *Tectonophysics*, 607, 51–64. <https://doi.org/10.1016/j.tecto.2013.05.041>
- Autin, J., Leroy, S., Beslier, M. O., D'Acremont, E., Razin, P., Ribodetti, A., et al. (2010). Continental break-up history of a deep magma-poor margin based on seismic reflection data (northeastern Gulf of Aden margin, offshore Oman). *Geophysical Journal International*, 180(2), 501–519. <https://doi.org/10.1111/j.1365-246X.2009.04424.x>
- Bellahsen, N., Husson, L., Autin, J., Leroy, S., & D'Acremont, E. (2013). The effect of thermal weakening and buoyancy forces on rift localization: Field evidences from the Gulf of Aden oblique rifting. *Tectonophysics*, 607, 80–97. <https://doi.org/10.1016/j.tecto.2013.05.042>
- Beyene, A., & Abdelsalam, M. G. (2005). Tectonics of the Afar depression: A review and synthesis. *Journal of African Earth Sciences*, 41(1–2), 41–59. <https://doi.org/10.1016/j.jafrearsci.2005.03.003>
- Bohannon, R. G., & Eittreim, S. L. (1991). Tectonic development of passive continental margins of the southern and central Red Sea with a comparison to Wilkes Land, Antarctica. *Tectonophysics*, 198(2–4), 129–154. [https://doi.org/10.1016/0040-1951\(91\)90148-L](https://doi.org/10.1016/0040-1951(91)90148-L)
- Bonnemains, D., Carlut, J., Escartín, J., Mével, C., Andreani, M., & Debret, B. (2016). Magnetic signatures of serpentinization at ophiolite complexes. *Geochemistry, Geophysics, Geosystems*, 17(8), 2969–2986. <https://doi.org/10.1002/2016GC006321>
- Bosworth, W., Huchon, P., & McClay, K. (2005). The Red Sea and Gulf of Aden Basins. *Journal of African Earth Sciences*, 43(1–3), 334–378. <https://doi.org/10.1016/j.jafrearsci.2005.07.020>
- Bosworth, W., & Stockli, D. F. (2016). Early magmatism in the greater Red Sea rift: Timing and significance. *Canadian Journal of Earth Sciences*, 53(11), 1158–1176. <https://doi.org/10.1139/cjes-2016-0019>
- Brune, S., & Autin, J. (2013). The rift to break-up evolution of the Gulf of Aden: Insights from 3D numerical lithospheric-scale modelling. *Tectonophysics*, 607, 65–79. <https://doi.org/10.1016/j.tecto.2013.06.029>
- Brune, S., Heine, C., Clift, P. D., & Pérez-Gussinyé, M. (2017). Rifted margin architecture and crustal rheology: Reviewing Iberia-Newfoundland, Central South Atlantic, and South China Sea. *Marine and Petroleum Geology*, 79, 257–281. <https://doi.org/10.1016/j.marpetgeo.2016.10.018>
- Brune, S., Popov, A. A., & Sobolev, S. V. (2013). Quantifying the thermo-mechanical impact of plume arrival on continental break-up. *Tectonophysics*, 604, 51–59. <https://doi.org/10.1016/j.tecto.2013.02.009>
- Buck, W. R. (1991). Modes of continental lithospheric extension. *Journal of Geophysical Research*, 96(B12), 20161–20178. <https://doi.org/10.1029/91jb01485>
- Buiter, S. (2014). How plumes help to break plates. *Nature*, 513(7516), 36–37. <https://doi.org/10.1038/513036a>
- Carbotte, S. M. (2005). Seismic structure at Mid-Ocean ridges. In *Encyclopedia of geology* (pp. 405–417). Elsevier. <https://doi.org/10.1016/b0-12-369396-9/00449-4>
- Celli, N. L., Lebedev, S., Schaeffer, A. J., & Gaina, C. (2020). African cratonic lithosphere carved by mantle plumes. *Nature Communications*, 11(1), 1–10. <https://doi.org/10.1038/s41467-019-13871-2>.
- Chappell, A. R., & Kusznir, N. J. (2008). Three-dimensional gravity inversion for Moho depth at rifted continental margins incorporating a lithosphere thermal gravity anomaly correction. *Geophysical Journal International*, 174, 1–13. <https://doi.org/10.1111/j.1365-246X.2008.03803.x>
- Clerc, C., Lagabrielle, Y., Labaume, P., Ringenbach, J. C., Vauchez, A., Nalpas, T., et al. (2016). Basement – Cover decoupling and progressive exhumation of metamorphic sediments at hot rifted margin. Insights from the Northeastern Pyrenean analog. *Tectonophysics*, 686, 82–97. <https://doi.org/10.1016/j.tecto.2016.07.022>
- Clerc, C., Ringenbach, J. C., Jolivet, L., & Ballard, J. F. (2018). Rifted margins: Ductile deformation, boudinage, continentward-dipping normal faults and the role of the weak lower crust. *Gondwana Research*, 53, 20–40. <https://doi.org/10.1016/j.gr.2017.04.030>

- Cochran, J. R. (1983). A model for development of Red Sea. *American Association of Petroleum Geologists Bulletin*, 67, 41–69. <https://doi.org/10.1306/03b5acbe-16d1-11d7-8645000102c1865d>
- Cochran, J. R. (2005). Northern Red Sea: Nucleation of an oceanic spreading center within a continental rift. *Geochemistry, Geophysics, Geosystems*, 6(3). <https://doi.org/10.1029/2004GC000826>
- Courtillot, V., Jaupart, C., Manighetti, I., Tapponnier, P., & Besse, J. (1999). On causal links between flood basalts and continental breakup. *Earth and Planetary Science Letters*, 166(3–4), 177–195. [https://doi.org/10.1016/S0012-821X\(98\)00282-9](https://doi.org/10.1016/S0012-821X(98)00282-9)
- Dang, Z., Zhang, N., Li, Z.-X., Huang, C., Spencer, C. J., & Liu, Y. (2020). Weak orogenic lithosphere guides the pattern of plume-triggered supercontinent break-up. *Communications Earth & Environment*, 1, 1–11. <https://doi.org/10.1038/s43247-020-00052-z>
- Davison, I., Al Kadasi, M., Al-Khirubash, M., Al-Subbary, A. K., Baker, J., Blakey, S., et al. (1994). Geological evolution of the southeastern Red Sea Rift margin, Republic of Yemen. *Geological Society of America Bulletin*, 106, 1474–1493. [https://doi.org/10.1130/0016-7606\(1994\)106<1474:GEOTSR>2.3.CO;2](https://doi.org/10.1130/0016-7606(1994)106<1474:GEOTSR>2.3.CO;2)
- DeMets, C., & Merkouriev, S. (2016). High-resolution estimates of Nubia-Somalia plate motion since 20 Ma from reconstructions of the Southwest Indian Ridge, Red Sea and Gulf of Aden. *Geophysical Journal International*, 207(1), 317–332. <https://doi.org/10.1093/gji/ggw276>
- Egloff, F., Rihm, R., Makris, J., Izzeldin, Y. A., Bobsien, M., Meier, K., et al. (1991). Contrasting structural styles of the eastern and western margins of the southern Red Sea: The 1988 SONNE experiment. *Tectonophysics*, 198(2–4), 329–353. [https://doi.org/10.1016/0040-1951\(91\)90159-P](https://doi.org/10.1016/0040-1951(91)90159-P)
- El-Isa, Z. H. (2015). Seismicity and seismotectonics of the Red Sea Region. *Arabian Journal of Geosciences*, 8(10), 8505–8525. <https://doi.org/10.1007/s12517-015-1819-2>
- El Khrepy, S., Koulakov, I., Gerya, T., Al-Arifi, N., Alajmi, M. S., & Qadrouh, A. N. (2021). Transition from continental rifting to oceanic spreading in the northern Red Sea area. *Scientific Reports*, 11, 1–7. <https://doi.org/10.1038/s41598-021-84952-w>
- Faccenna, C., Becker, T. W., Jolivet, L., & Keskin, M. (2013). Mantle convection in the Middle East: Reconciling Afar upwelling, Arabia indentation and Aegean trench rollback. *Earth and Planetary Science Letters*, 375, 254–269. <https://doi.org/10.1016/j.epsl.2013.05.043>
- Fischer, K. M., Ford, H. A., Abt, D. L., & Rychert, C. A. (2010). The lithosphere-asthenosphere boundary. *Annual Review of Earth and Planetary Sciences*, 38(1), 551–575. <https://doi.org/10.1146/annurev-earth-040809-152438>
- Follmann, J., van der Zwan, F. M., Preine, J., Hübscher, C., Bousquet, R., & Augustin, N. (2021). Gabbro discovery in discovery deep: First Plutonic Rock samples from the Red Sea Rift axis. *Frontiers of Earth Science*, 9, 957. <https://doi.org/10.3389/feart.2021.742815>
- Fournier, M., Chamot-Rooke, N., Petit, C., Huchon, P., Al-Kathiri, A., Audin, L., et al. (2010). Arabia-Somalia plate kinematics, evolution of the Aden-Owen-Carlsberg triple junction, and opening of the Gulf of Aden. *Journal of Geophysical Research*, 115(B4), 1–24. <https://doi.org/10.1029/2008JB006257>
- François, T., Koptev, A., Cloetingh, S., Burov, E., & Gerya, T. (2018). Plume-lithosphere interactions in rifted margin tectonic settings: Inferences from thermo-mechanical modelling. *Tectonophysics*, 746, 138–154. <https://doi.org/10.1016/j.tecto.2017.11.027>
- Fullea, J., Lebedev, S., Martinez, Z., & Celli, N. L. (2021). WINTERC-G: Mapping the upper mantle thermochemical heterogeneity from coupled geophysical–petrological inversion of seismic waveforms, heat flow, surface elevation and gravity satellite data. *Geophysical Journal International*, 226(1), 146–191. <https://doi.org/10.1093/gji/ggab094>
- Furman, T., Bryce, J., Rooney, T., Hanan, B., Yirgu, G., & Ayalew, D. (2006). Heads and tails: 30 million years of the Afar plume. *Geological Society Special Publication*, 259, 95–119. <https://doi.org/10.1144/GSL.SP.2006.259.01.09>
- Gallacher, R., Keir, D., & Harmon, N. (2019). The nature of upper mantle upwelling during initiation of Seafloor Spreading in the Southern Red Sea. In *Geological setting, palaeoenvironment and archaeology of the Red Sea* (pp. 113–129). Springer International Publishing. https://doi.org/10.1007/978-3-319-99408-6_6
- Gallacher, R. J., Keir, D., Harmon, N., Stuart, G., Leroy, S., Hammond, J. O. S., et al. (2016). The initiation of segmented buoyancy-driven melting during continental breakup. *Nature Communications*, 7, 1–9. <https://doi.org/10.1038/ncomms13110>
- Gaulier, J., Le Pichon, X., Lyberis, N., Avedik, F., Geli, L., Moretti, I., et al. (1988). Seismic study of the crust of the northern Red Sea and Gulf of Suez. *Tectonophysics*, 153(1–4), 55–88. [https://doi.org/10.1016/0040-1951\(88\)90007-8](https://doi.org/10.1016/0040-1951(88)90007-8)
- GEBCO Compilation Group. (2021). The GEBCO_2019 grid: A continuous terrain model of the global oceans and land. <https://doi.org/10.5285/c6612cbe-50b3-0c9f-e053-6c86abc09f8f>
- Geoffroy, L. (2005). Volcanic passive margins. *Comptes Rendus Geoscience*, 337(16), 1395–1408. <https://doi.org/10.1016/j.crte.2005.10.006>
- Gillard, M., Leroy, S., Cannat, M., & Sloan, H. (2021). Margin-to-Margin seafloor spreading in the Eastern Gulf of Aden: A 16 Ma-long history of deformation and magmatism from Seismic reflection, Gravity and magnetic data. *Frontiers of Earth Science*, 9, 628. <https://doi.org/10.3389/feart.2021.707721>
- Götze, H. J., & Lahmeyer, B. (1988). Application of three-dimensional interactive modeling in gravity and magnetics. *Geophysics*, 53(8), 1096–1108. <https://doi.org/10.1190/1.1442546>
- Haase, C. (2008). *Inversion of gravity, gravity gradient, and magnetic data with application to subsalt imaging* (p. 83). Christian-Albrechts-Universität zu Kiel.
- Haase, C., & Ebbing, J. (2013). *Complete Bouguer correction-Statoil database offshore Mid-Norway*. Report no. 2013.038. Geological Survey of Norway.
- Haase, K. M., Mühe, R., & Stoffers, P. (2000). Magmatism during extension of the lithosphere: Geochemical constraints from lavas of the Shaban Deep, northern Red Sea. *Chemical Geology*, 166(3–4), 225–239. [https://doi.org/10.1016/S0009-2541\(99\)00221-1](https://doi.org/10.1016/S0009-2541(99)00221-1)
- Hall, S. A. (1989). Magnetic evidence for the nature of the crust beneath the southern Red Sea. *Journal of Geophysical Research*, 94(B9), 267–279. <https://doi.org/10.1029/jb094ib09p12267>
- Hansen, S. E., Gaherty, J. B., Schwartz, S. Y., Rodgers, A. J., & Al-Amri, A. M. S. (2008). Seismic velocity structure and depth-dependence of anisotropy in the Red Sea and Arabian shield from surface wave analysis. *Journal of Geophysical Research*, 113(B10), B10307. <https://doi.org/10.1029/2007JB005335>
- Hansen, S. E., Rodgers, A. J., Schwartz, S. Y., & Al-Amri, A. M. S. (2007). Imaging ruptured lithosphere beneath the Red Sea and Arabian Peninsula. *Earth and Planetary Science Letters*, 259(3–4), 256–265. <https://doi.org/10.1016/j.epsl.2007.04.035>
- Huismans, R., & Beaumont, C. (2011). Depth-dependent extension, two-stage breakup and cratonic underplating at rifted margins. *Nature*, 473(7345), 74–78. <https://doi.org/10.1038/nature09988>
- Huismans, R., & Beaumont, C. (2014). Rifted continental margins: The case for depth-dependent extension. *Earth and Planetary Science Letters*, 407, 148–162. <https://doi.org/10.1016/j.epsl.2014.09.032>
- Hyndman, R. D., & Peacock, S. M. (2003). Serpentinization of the forearc mantle. *Earth and Planetary Science Letters*, 212(3–4), 417–432. [https://doi.org/10.1016/S0012-821X\(03\)00263-2](https://doi.org/10.1016/S0012-821X(03)00263-2)
- Ince, E. S., Barthelmes, F., Reißland, S., Elger, K., Förste, C., Flechtner, F., & Schuh, H. (2019). ICGEM – 15 years of successful collection and distribution of global gravitational models, associated services, and future plans. *Earth System Science Data*, 11(2), 647–674. <https://doi.org/10.5194/essd-11-647-2019>

- Issachar, R., Ebbing, J., & Dilixiati, Y. (2022). New magnetic anomaly map for the Red Sea reveals transtensional structures associated with rotational rifting. *Scientific Reports*, *12*, 1–13. <https://doi.org/10.1038/s41598-022-09770-0>
- Issachar, R., Gómez-García, Á. M., & Ebbing, J. (2022). *Rift architecture of the Red Sea from four end-member scenarios*. GFZ Data Service. <https://doi.org/10.5880/GFZ.4.5.2022.006>
- Izzeldin, A. Y. (1987). Seismic, gravity and magnetic surveys in the central part of the Red Sea: Their interpretation and implications for the structure and evolution of the Red Sea. *Tectonophysics*, *143*(4), 269–306. [https://doi.org/10.1016/0040-1951\(87\)90214-9](https://doi.org/10.1016/0040-1951(87)90214-9)
- Kelemen, P. B., & Holbrook, W. S. (1995). Origin of thick, high-velocity igneous crust along the US East Coast margin. *Journal of Geophysical Research*, *100*(B6), 10077–10094. <https://doi.org/10.1029/95jb00924>
- Klingelhöfer, F., Géli, L., Matias, L., Steinsland, N., & Mohr, J. (2000). Crustal structure of a super-slow spreading centre: A seismic refraction study of Mohs Ridge, 72°N. *Geophysical Journal International*, *141*(2), 509–526. <https://doi.org/10.1046/j.1365-246X.2000.00098.x>
- Koptev, A., Calais, E., Burov, E., Leroy, S., & Gerya, T. (2015). Dual continental rift systems generated by plume-lithosphere interaction. *Nature Geoscience*, *8*(5), 388–392. <https://doi.org/10.1038/ngeo2401>
- Koptev, A., Cloetingh, S., Burov, E., François, T., & Gerya, T. (2017). Long-distance impact of Iceland plume on Norway's rifted margin. *Scientific Reports*, *7*, 1–11. <https://doi.org/10.1038/s41598-017-07523-y>
- Lagabriele, Y., Clerc, C., Vauchez, A., Lahfid, A., Labaume, P., Azambre, B., et al. (2016). Very high geothermal gradient during mantle exhumation recorded in mylonitic marbles and carbonate breccias from a Mesozoic Pyrenean palaeomargin (Lherz area, North Pyrenean Zone, France). *Comptes Rendus Geoscience*, *348*(3–4), 290–300. <https://doi.org/10.1016/j.crte.2015.11.004>
- Ligi, M., Bonatti, E., Bosworth, W., & Ronca, S. (2019). Oceanization starts at depth during continental rifting in the Northern Red Sea. In *Geological setting, palaeoenvironment and archaeology of the Red Sea* (pp. 131–157). Springer International Publishing. https://doi.org/10.1007/978-3-319-99408-6_7
- Liu, Y., Li, C. F., Wen, Y., Yao, Z., Wan, X., Qiu, X., et al. (2021). Mantle serpentinization beneath a failed rift and post-spreading magmatism in the northeastern South China Sea margin. *Geophysical Journal International*, *225*(2), 811–828. <https://doi.org/10.1093/gji/ggab006>
- Lowell, J. D., & Geni, G. J. (1972). Sea-floor spreading and structural evolution of Southern Red Sea. *AAPG Bulletin*, *56*, 247–259. <https://doi.org/10.1306/819a3e56-16c5-11d7-8645000102c1865d>
- Mai, P. M., Julià, J., & Tang, Z. (2019). Crustal and upper-mantle structure beneath Saudi Arabia from receiver functions and surface wave analysis. In *Geological setting, palaeoenvironment and archaeology of the Red Sea* (pp. 307–322). https://doi.org/10.1007/978-3-319-99408-6_14
- Makris, J., & Ginzburg, A. (1987). The Afar depression: Transition between continental rifting and sea-floor spreading. *Tectonophysics*, *141*(1–3), 199–214. [https://doi.org/10.1016/0040-1951\(87\)90186-7](https://doi.org/10.1016/0040-1951(87)90186-7)
- Manighetti, I., Tapponnier, P., Courtillot, V., Gruszow, S., & Gillot, P.-Y. (1997). Propagation of rifting along the Arabia-Somalia plate boundary: The Gulfs of Aden and Tadjoura. *Journal of Geophysical Research*, *102*(B2), 2681–2710. <https://doi.org/10.1029/96jb01185>
- Mitchell, N. C., & Sofianos, S. S. (2018). Origin of submarine channel North of Hanish Sill, Red Sea. In *Geological setting, palaeoenvironment and archaeology of the Red Sea* (pp. 259–273). Springer International Publishing. https://doi.org/10.1007/978-3-319-99408-6_12
- Mitchell, N. C., & Stewart, I. C. F. (2018). The modest seismicity of the northern Red Sea rift. *Geophysical Journal International*, *214*(3), 1507–1523. <https://doi.org/10.1093/GJI/GGY176>
- Molnar, N., Cruden, A., & Betts, P. (2020). The role of inherited crustal and lithospheric architecture during the evolution of the Red Sea: Insights from three dimensional analogue experiments. *Earth and Planetary Science Letters*, *544*, 116377. <https://doi.org/10.1016/j.epsl.2020.116377>
- Mooney, W. D., Gettings, M. E., Blank, H. R., & Healy, J. H. (1985). Saudi Arabian seismic-refraction profile: A traveltimes interpretation of crustal and upper mantle structure. *Tectonophysics*, *111*(3–4), 173–246. [https://doi.org/10.1016/0040-1951\(85\)90287-2](https://doi.org/10.1016/0040-1951(85)90287-2)
- Mooney, W. D., & Kaban, M. K. (2010). The North American upper mantle: Density, composition, and evolution. *Journal of Geophysical Research*, *115*(B12), 12424. <https://doi.org/10.1029/2010JB000866>
- Morag, N., Haviv, I., Eyal, M., Kohn, B. P., & Feinstein, S. (2019). Early flank uplift along the Suez rift: Implications for the role of mantle plumes and the onset of the Dead Sea transform. *Earth and Planetary Science Letters*, *516*, 56–65. <https://doi.org/10.1016/j.epsl.2019.03.002>
- Moreira, M., Valbracht, P. J., Staudacher, T., & Allègre, C. J. (1996). Rare gas systematics in Red Sea ridge basalts. *Geophysical Research Letters*, *23*(18), 2453–2456. <https://doi.org/10.1029/96GL02301>
- Morgan, W. J. (1971). Convection plumes in the lower mantle. *Nature*, *230*(5288), 42–43. <https://doi.org/10.1038/230042a0>
- Moulin, M., Aslanian, D., Olivet, J. L., Contrucci, I., Matias, L., Géli, L., et al. (2005). Geological constraints on the evolution of the Angolan margin based on reflection and refraction seismic data (ZaïAngo project). *Geophysical Journal International*, *162*(3), 793–810. <https://doi.org/10.1111/j.1365-246X.2005.02668.x>
- Park, Y., Nyblade, A. A., Park, Y., Nyblade, A. A., Rodgers, A. J., & Al-Amri, A. (2008). S wave velocity structure of the Arabian Shield upper mantle from Rayleigh wave tomography. *Geochemistry, Geophysics, Geosystems*, *9*(7), 1213. <https://doi.org/10.1029/2007GC001895>
- Perfit, M. R. (2001). Mid-Ocean ridge geochemistry and petrology. In *Encyclopedia of Ocean sciences* (pp. 815–825). Academic Press. <https://doi.org/10.1016/B978-012374473-9.00096-5>
- Péron-Pinvidic, G., & Manatschal, G. (2009). The final rifting evolution at deep magma-poor passive margins from Iberia-Newfoundland: A new point of view. *International Journal of Earth Sciences*, *98*(7), 1581–1597. <https://doi.org/10.1007/s00531-008-0337-9>
- Péron-Pinvidic, G., Manatschal, G., Masini, E., Sutra, E., Flament, J. M., Hauptert, I., & Unternehr, P. (2017). *Unravelling the along-strike variability of the Angola-Gabon rifted margin: A mapping approach* (Vol. 438, pp. 49–76). Geological Society Special Publication. <https://doi.org/10.1144/SP438.1>
- Plaziat, J.-C., Baltzer, F., Choukri, A., Conchon, O., Freyret, P., Orszag-Sperber, F., et al. (1998). Quaternary marine and continental sedimentation in the northern Red Sea and Gulf of Suez (Egyptian coast): Influences of rift tectonics, climatic changes and sea-level fluctuations. In *Sedimentation and Tectonics in rift basins Red Sea- Gulf of Aden* (pp. 537–573). Springer. https://doi.org/10.1007/978-94-011-4930-3_29
- Poudjom Djomani, Y. H., O'Reilly, S. Y., Griffin, W. L., & Morgan, P. (2001). The density structure of subcontinental lithosphere through time. *Earth and Planetary Science Letters*, *184*(3–4), 605–621. [https://doi.org/10.1016/S0012-821X\(00\)00362-9](https://doi.org/10.1016/S0012-821X(00)00362-9)
- Prave, A. R., Bates, C. R., Donaldson, C. H., Toland, H., Condon, D. J., Mark, D., & Raub, T. D. (2016). Geology and geochronology of the Tana basin, Ethiopia: LIP volcanism, Super eruptions and Eocene-Oligocene environmental change. *Earth and Planetary Science Letters*, *443*, 1–8. <https://doi.org/10.1016/j.epsl.2016.03.009>
- Ravat, D., Salem, A., Abdelaziz, A. M. S., Elawadi, E., & Morgan, P. (2011). Probing magnetic bottom and crustal temperature variations along the Red Sea margin of Egypt. *Tectonophysics*, *510*(3–4), 337–344. <https://doi.org/10.1016/j.tecto.2011.08.002>
- Reguzzoni, M., & Sampietro, D. (2015). GEMMA: An Earth crustal model based on GOCE satellite data. *International Journal of Applied Earth Observation and Geoinformation*, *35*, 31–43. <https://doi.org/10.1016/j.jag.2014.04.002>
- Reilinger, R., McClusky, S., Vernant, P., Lawrence, S., Ergintav, S., Cakmak, R., et al. (2006). GPS constraints on continental deformation in the Africa-Arabia-Eurasia continental collision zone and implications for the dynamics of plate interactions. *Journal of Geophysical Research: Solid Earth*, *111*(B5). <https://doi.org/10.1029/2005jb004051>

- Rüpke, L. H., Schmid, D. W., Perez-Gussinye, M., & Hartz, E. (2013). Interrelation between rifting, faulting, sedimentation, and mantle serpentinization during continental margin formation - including examples from the Norwegian Sea. *Geochemistry, Geophysics, Geosystems*, *14*(10), 4351–4369. <https://doi.org/10.1002/ggge.20268>
- Saada, S. A., Mickus, K., Eldosouky, A. M., & Ibrahim, A. (2021). Insights on the tectonic styles of the Red Sea rift using gravity and magnetic data. *Marine and Petroleum Geology*, *133*, 105253. <https://doi.org/10.1016/j.marpetgeo.2021.105253>
- Saleh, S., Jahr, T., Jentzsch, G., Saleh, A., & Ashour, N. M. A. (2006). Crustal evaluation of the northern Red Sea Rift and Gulf of Suez, Egypt from geophysical data: 3-dimensional modeling. *Journal of African Earth Sciences*, *45*(3), 257–278. <https://doi.org/10.1016/j.jafrearsci.2006.02.001>
- Sapin, F., Ringenbach, J. C., & Clerc, C. (2021). Rifted margins classification and forcing parameters. *Scientific Reports*, *11*, 1–17. <https://doi.org/10.1038/s41598-021-87648-3>
- Schettino, A., Macchiavelli, C., Pierantoni, P. P., Zanoni, D., & Rasul, N. (2016). Recent kinematics of the tectonic plates surrounding the Red Sea and Gulf of Aden. *Geophysical Journal International*, *207*(1), 457–480. <https://doi.org/10.1093/gji/ggw280>
- Schmidt, S., Anikiev, D., Götz, H. J., Gomez Garcia, A., Meeßen, C., Plonka, C., et al. (2020). 3D potential field modelling of complex geological structures (p. EGU2020-8383). Copernicus Meetings. <https://doi.org/10.5194/egusphere-egu2020-8383>
- Schmidt, S., Plonka, C., Götz, H. J., & Lahmeyer, B. (2011). Hybrid modelling of gravity, gravity gradients and magnetic fields. *Geophysical Prospecting*, *59*(6), 1046–1051. <https://doi.org/10.1111/j.1365-2478.2011.00999.x>
- Stern, R. J., & Johnson, P. R. (2018). Constraining the opening of the red sea: Evidence from the neoproterozoic margins and cenozoic magmatism for a volcanic rifted margin. In *Geological setting, palaeoenvironment and archaeology of the Red Sea* (pp. 53–79). Springer International Publishing. https://doi.org/10.1007/978-3-319-99408-6_4
- Stockli, D. F., & Bosworth, W. B. (2018). Timing of extensional faulting along the magma-poor central and northern red sea rift margin-transition from regional extension to necking along a hyperextended rifted margin. In *Geological setting, palaeoenvironment and archaeology of the Red Sea* (pp. 81–111). Springer International Publishing. https://doi.org/10.1007/978-3-319-99408-6_5
- Storey, B. C. (1995). The role of mantle plumes in continental breakup: Case histories from Gondwanaland. *Nature*, *377*(6547), 301–308. <https://doi.org/10.1038/377301a0>
- Straume, E. O., Gaina, C., Medvedev, S., Hochmuth, K., Gohl, K., Whittaker, J. M., et al. (2019). GlobSed: Updated total sediment thickness in the World's Oceans. *Geochemistry, Geophysics, Geosystems*, *20*(4), 1756–1772. <https://doi.org/10.1029/2018GC008115>
- Szwilius, W., Afonso, J. C., Ebbing, J., & Mooney, W. D. (2019). Global crustal thickness and velocity structure from geostatistical analysis of seismic data. *Journal of Geophysical Research: Solid Earth*, *124*(2), 1626–1652. <https://doi.org/10.1029/2018JB016593>
- Szymanski, E., Stockli, D. F., Johnson, P. R., & Hager, C. (2016). Thermochronometric evidence for diffuse extension and two-phase rifting within the Central Arabian Margin of the Red Sea Rift. *Tectonics*, *35*(12), 2863–2895. <https://doi.org/10.1002/2016TC004336>
- Theissen, S., & Rüpke, L. H. (2010). Feedbacks of sedimentation on crustal heat flow: New insights from the Vøring Basin. *Norwegian Sea: Basin Research*, *22*, 976–990. <https://doi.org/10.1111/j.1365-2117.2009.00437.x>
- Toft, P. B., Arkani-Hamed, J., & Haggerty, S. E. (1990). The effects of serpentinization on density and magnetic susceptibility: A petrophysical model. *Physics of the Earth and Planetary Interiors*, *65*(1–2), 137–157. [https://doi.org/10.1016/0031-9201\(90\)90082-9](https://doi.org/10.1016/0031-9201(90)90082-9)
- Unterneh, P., Péron-Pinvidic, G., Manatschal, G., & Sutra, E. (2010). Hyper-extended crust in the South Atlantic: In search of a model. *Petroleum Geoscience*, *16*(3), 207–215. <https://doi.org/10.1144/1354-079309-904>
- USGS. (2021). Google Earth™ KML files. Retrieved from <https://www.usgs.gov/programs/earthquake-hazards/google-earthkml-files>
- van der Zwan, F. M., Devey, C. W., Augustin, N., Almeev, R. R., Bantan, R. A., & Basaham, A. (2015). Hydrothermal activity at the ultraslow-to slow-spreading Red Sea Rift traced by chlorine in basalt. *Chemical Geology*, *405*, 63–81. <https://doi.org/10.1016/j.chemgeo.2015.04.001>
- Varet, J. (1978). *Geology of central and southern Afar (Ethiopia and Djibouti Republic)*. Centre national de la recherche scientifique.
- Viltres, R., Jónsson, S., Ruch, J., Doubré, C., Reilinger, R., Floyd, M., & Ogubazghi, G. (2020). Kinematics and deformation of the southern Red Sea region from GPS observations. *Geophysical Journal International*, *221*(3), 2143–2154. <https://doi.org/10.1093/gji/ggaa109>
- Voggenreiter, W., Hötzl, H., & Mechie, J. (1988). Low-angle detachment origin for the Red Sea Rift system? *Tectonophysics*, *150*(1–2), 51–75. [https://doi.org/10.1016/0040-1951\(88\)90295-8](https://doi.org/10.1016/0040-1951(88)90295-8)
- Yao, Z., Mooney, W. D., Zahran, H. M., & Youssef, S. E. H. (2017). Upper mantle velocity structure beneath the Arabian shield from Rayleigh surface wave tomography and its implications. *Journal of Geophysical Research: Solid Earth*, *122*(8), 6552–6568. <https://doi.org/10.1002/2016JB013805>
- Zingerle, P., Pail, R., Gruber, T., & Oikonomidou, X. (2020). The combined global gravity field model XGM2019e. *Journal of Geodesy*, *94*(7), 1–12. <https://doi.org/10.1007/S00190-020-01398-0>